

STUDY OF CREEP OF ALUMINA-FORMING AUSTENITIC STAINLESS STEEL  
FOR HIGH-TEMPERATURE ENERGY APPLICATIONS

A Thesis  
Submitted to the Faculty  
in partial fulfillment of the requirements for the  
degree of  
Master of Science  
by

NATALIE PETROVNA AFONINA

Thayer School of Engineering  
Dartmouth College  
Hanover, New Hampshire  
Date that submit signed thesis

Examining Committee:

Chairman \_\_\_\_\_  
(Dr. Ian Baker)  
Member \_\_\_\_\_  
(Dr. Harold Frost)  
Member \_\_\_\_\_  
(Dr. Rachel Obbard)

---

F. Jon Kull  
Dean of Graduate Studies



## ABSTRACT

To withstand the high temperature ( $>700^{\circ}\text{C}$ ) and pressure demands of steam turbines and boilers used for energy applications, metal alloys must be economically viable and have the necessary material properties, such as high-temperature creep strength, oxidation and corrosion resistance, to withstand such conditions. One promising class of alloys potentially capable of withstanding the rigors of aggressive environments, are alumina-forming austenitic stainless steels (AFAs) alloyed with aluminum to improve corrosion and oxidation resistance. The effect of aging on the microstructure, high temperature constant-stress creep behavior and mechanical properties of the AFA-type alloy Fe-20Cr-30Ni-2Nb-5Al (at.%) were investigated in this study.

The alloy's microstructural evolution with increased aging time was observed prior to creep testing. As aging time increased, the alloy exhibited increasing quantities of fine  $\text{Fe}_2\text{Nb}$  Laves phase dispersions, with a precipitate-free zone appearing in samples with higher aging times. The presence of the  $\text{L}1_2$  phase  $\gamma^{\prime}$ - $\text{Ni}_3\text{Al}$  precipitate was detected in the alloy's matrix at  $760^{\circ}\text{C}$ .

A constant-stress creep rig was designed, built and its operation validated. Constant-stress creep tests were performed at  $760^{\circ}\text{C}$  and 35MPa, and the effects of different aging conditions on creep rate were investigated. Specimens aged for 240 h exhibited the highest creep rate by a factor of 5, with the homogenized sample having the second highest rate. Samples aged for 2.4 h and 24 h exhibited similar low secondary

creep rates. Creep tests conducted at 700°C exhibited a significantly lower creep rate compared to those at 760°C.

Microstructural analysis was performed on crept samples to explore high temperature straining properties. The quantity and size of  $\text{Fe}_2\text{Nb}$  Laves phase and NiAl particles increased in the matrix and on grain boundaries with longer aging time.

High temperature tensile tests were performed and compared to room temperature results. The high temperature results were significantly lower when compared to room temperature values. Higher creep rates were correlated with lower yield strengths.

## ACKNOWLEDGEMENTS

I would like to thank:

My adviser Professor Ian Baker, whose patience, expertise, unwavering support and encouragement made it possible for me to complete my studies.

The Baker Lab Research Group for their support and guidance.

The Carpenter Technology Corporation for providing test material for this study.

The Thayer School of Engineering Instrument Room staff for teaching me how to wire electronics properly and avoid shocking myself.

Claire Stolz, for the pep talks worthy of rousing armies and accompanying me on moonlit Methow walks. Without you by my side the cougars would've gotten me.

Nate Beatty, for being there in the darkest hour, for sharing a love of micro-adventures and always having my back.

Mark Fischer, for being a watchful older brother and lending a new perspective. You've kept me successfully out of trouble most of the time.

Julian Childs-Walker, for being my twin and remaining the only person to ever hitchhike past the Arctic Circle to adventure with me. You've continuously helped me get up to no good and our conversations help me make sense of this world.

I can't convey how much I owe my family for getting me this far.

My sister Jane Bellousov for being the level-headed one in the family and your incredible resilience. I can't wait to go on more adventure trips with you as we grow older together.

My father Yevgeniy Belousov, for encouraging me to stop working so hard and go on more climbing breaks outside. You've provided much needed perspective and inspiration.

My grandmother Dr. Galina Gataulina for worrying about my academic timeline, encouraging me not to procrastinate and feeding me delicious piroshki.

My grandfather Dr. Akhiyar Myginovich for reminding me that life can be filled with meaningful work and to never lose your inner child wonder of how the world works. For always being proud and supportive and teaching me how to use a crowbar to pull nails and lay bricks in a straight line. You encouraged me on my path to graduate school, and I wish you'd still be here to see me complete what I started.

Most importantly, my mother Dr. Irina Afonina, without whom I would not be here today. Who supported me at every step from the moment the two of us immigrated to the United States from Russia. You gave me room to figure things out on my own and spread my wings. You sadly left us before I could finish this thesis, but I know you would've been proud of me and would have loved to do the first round of edits.

*I dedicate this thesis to my mother.*

*Your support, unconditional love and sacrifices are responsible for everything I've accomplished.*

## **TABLE OF CONTENTS**

## **LIST OF TABLES**

## **LIST OF FIGURES**

Figure 1: Abc .....	15
Figure 2: Abc.....	27

## CHAPTER 1 INTRODUCTION

### 1.1 Background

Increasing efficiency while decreasing the cost of operating advanced power plants has been an ongoing process. Energy efficiency gains in fossil energy conversion and combustion system applications also result in the added benefit of reducing CO<sub>2</sub> emissions, bolstering the motivation to pursue efficiency-increasing strategies <sup>1-4</sup>. The efficiency of energy conversion applications is a strong function of steam temperature and pressure, thus increases in energy efficiency can be realized by elevating operating steam temperatures and pressures <sup>5</sup>. An increase in operating temperatures from 600°C to 800°C results in an efficiency increase of more than 10%. Most current coal power plants in the U.S. operate at a maximum steam temperature of 538°C <sup>6</sup>. Advanced ultrasupercritical steam boilers and turbines for power plants offer the promise of higher efficiencies and lower emissions, which are goals of the U.S. Department of Energy's Advanced Power Systems Initiatives. Efforts are currently underway to enable advanced power plants to function at temperatures greater than 700°C <sup>7</sup>. Specifically, the U.S. Department of Energy has set a goal to develop materials technology needed for the construction of the critical components of coal-fired boilers and turbines that are capable of operating with steam at temperatures of 760°C and pressures of 35 MPa, which can reduce emissions, including CO<sub>2</sub>, by 20% or greater compared to today's U.S. power plant fleet <sup>7-9</sup>.

An important contributor to realizing these higher steam temperatures and pressures is the material composition of the power plants' industrial gas turbine components, super heater tubes and boilers <sup>10</sup>. Currently, many energy production and chemical processing plants operate at temperatures below 600°C due to the poor performance of martensitic and ferritic steel alloys at higher temperatures <sup>11</sup>. To withstand the high temperature and pressure demands of energy applications, metal alloys must have the necessary material properties to withstand such conditions. These properties include the materials' high-temperature long term creep strength, oxidation and corrosion resistance and strength. Aggressive environments, where metal components are exposed to water vapor, sulfur and carbon species, are a prime target for new materials being developed <sup>12</sup>.

Nickel-based superalloys and austenitic alloys with high nickel concentrations perform well and have the necessary creep strength and oxidation and corrosion resistance to withstand such conditions, but are prohibitively expensive and not economically viable except for use in specialized applications due to the high levels of nickel and nickel's cost <sup>3,4</sup>. Thus, other alloys are now being researched and developed that can withstand the demands of such energy conversion and combustion systems as well as to decrease reliance on costly nickel-based alloys. However, in order for an alternative to be viable, it must have the strength, long-term creep resistance and oxidation resistance close to or exceeding that of nickel-based alloys. One promising class of alloys that are low in cost and potentially capable of withstanding the rigors

placed on the materials by high temperature energy applications are alumina-forming austenitic stainless steels (AFAs)<sup>10, 13-19</sup>. However, more investigation is needed into the oxidation and corrosion resistance as well as the creep strength in order for this class of steels to be widely used as an alternative to nickel-based alloys.

## 1.2 Alumina-Forming Austenitic Stainless Steels

Extensive efforts are underway to improve the high-temperature strength, corrosion and oxidation resistance, and long-term creep resistance of AFAs, ideally at lower cost compared with currently used materials. Researchers at Oak Ridge National Laboratory have developed a new family of AFAs in the last few years that have yielded promising results for use with elevated temperatures above 700°C in aggressive environments<sup>12,14,18,20,21</sup>. These new AFAs being developed have a composition range of Fe-(12-35)Ni-(12-15)Cr-(2.5-4)Al-(0.6-3)Nb (wt %), and include alloying additions such as Al, Cr, Mn and Ni to maintain a single phase austenitic matrix microstructure<sup>18</sup>.

The alumina ( $\text{Al}_2\text{O}_3$ ) layer that forms in AFAs at temperatures between 600-900°C, acts as a protective barrier and increases the oxidation and corrosion resistance of the material. Austenitic steels without sufficient additions of aluminum use chromia ( $\text{Cr}_2\text{O}_3$ ) scales as a protective layer, but in environments with high concentrations of water vapor and other oxidizing agents, the chromia scales perform poorly. Relatively small amounts of aluminum additions to austenitic steels have the ability to form the protective alumina surface layer. It's been shown that these alumina scale formations remain stable at operating temperatures from 650-800°C, with the necessary oxidation

resistance in environments with water vapor present, making AFAs the preferred choice for use in low-cost, high-temperature structural materials <sup>10,13,22-26</sup>. Ferritic FeCrAl alloys have excellent oxidation and corrosion resistance at elevated temperatures, however at temperatures greater than 600°C their creep resistance does not meet expectations set by nickel-based alloys, a property that is attributed to their open body-centered-cubic (b.c.c) structure <sup>18</sup>.

Precipitates play a large role in determining the mechanical properties of an alloy. Both the type of precipitate and their distribution have an effect on an alloy's strength and creep resistance. Precipitate nucleation occurs due to the strain energy being lowered <sup>27</sup>. Precipitates nucleate preferentially on grain boundaries due to a larger strain energy reduction compared with precipitation occurring on dislocations, which has a higher activation energy <sup>28</sup>. The type, size, distribution and volume fraction all have an effect on the alloy's properties. The effect of various precipitates and their phases on creep strength in AFAs with a variety of alloying elements is still being explored to identify the optimum combination of alloys and precipitates for their use at elevated temperatures in the 600°C to 800°C range. Small changes in alloy composition and precipitate phases often result in a wide variation of creep strengths <sup>5,19,29</sup>.

### **1.3 AFA precipitates**

In the past, AFAs have primarily used MC carbides (with the metal primarily being niobium) or  $\gamma'$ -Ni<sub>3</sub>Al for their strength <sup>12,14</sup>. Particles that are ~10 nm in size are effective at increasing creep strength by pinning dislocations in the f.c.c. austenitic

matrix. However at elevated temperatures above 800°C, the carbide precipitates coarsen and dissolve <sup>30</sup>, making them unsuitable for strengthening purposes in elevated temperature applications. Newer grades of AFAs being developed have an austenitic face-centered-cubic matrix instead of a b.c.c matrix, and their elevated temperature creep resistance and strength is achieved through not only the existing MC carbides and  $\gamma'$ -Ni<sub>3</sub>Al (L1<sub>2</sub>) precipitates, but also Fe<sub>2</sub>Nb Laves phase and NiAl-type B2 precipitates

10,18,31-33

In various Ni-based and Fe-based superalloys, the L1<sub>2</sub>-ordered  $\gamma'$ -Ni<sub>3</sub>Al precipitates are used for their strengthening effects of improving high-temperature mechanical properties <sup>19,34</sup>. The f.c.c. structure of Ni<sub>3</sub>Al can be seen in Figure 1.1. In a 2008 study, superior creep resistance in the AFA alloy Fe-20Cr-30Ni-2Nb-5Al (at%) compared to the base alloy was attributed to the formation of a dense dispersion of 30 nm in diameter spherical Ni<sub>3</sub>Al precipitates observed in creep-rupture samples tested at 750°C under a 100 MPa load <sup>20</sup>. Although present at 750°C, Ni<sub>3</sub>Al precipitates were not found in Fe-20Cr-30Ni-2Nb-5Al (at%) at 800°C, negating the precipitates' strengthening effects at high temperatures exceeding 800°C <sup>35</sup>. The presence of Ni<sub>3</sub>Al precipitates in the temperature range between 750°C-800°C in the AFA Fe-20Cr-30Ni-2Nb-5Al (at%) alloy has not been evaluated.

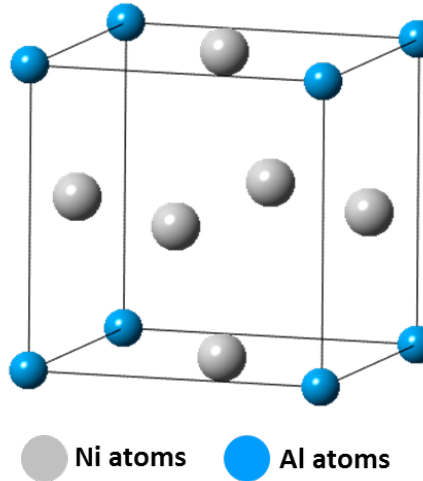


Figure 1.1: Diagram of the  $L1_2$ -ordered  $\gamma'$ - $Ni_3Al$  precipitate crystal structure.

Intermetallic precipitates have the potential to be used as strengtheners in AFA alloys to further improve their creep resistance. The formation of  $Fe_2Nb$  Laves phase precipitates along grain boundaries in ferritic steels results in a decrease in the alloys' toughness and yield strength<sup>36</sup>. In contrast, creep strengthening has been achieved in AFAs<sup>12,37</sup>. For example the AFA alloy Fe-20Cr-30Ni-2Nb-5Al (at%) demonstrates good ductility and strength, even with extensive intermetallic formation of  $Fe_2Nb$  Laves phase precipitates along the grain boundaries<sup>38</sup>. It has been shown that in Fe-20Cr-(25–35)Ni-2Nb (at%) alloys, fine dispersions of strengthening  $Fe_2Nb$  Laves phase can form within the austenitic iron matrix<sup>39</sup>. The use of  $Fe_2Nb$  Laves phase particles has shown thermal stability up to its melting point of 1640°C in the Fe-Nb system over a prolonged duration<sup>40</sup> and exists in equilibrium with f.c.c.  $\gamma$ -Fe above 955°C in the Fe-Cr-Ni base steel<sup>41</sup>, making it a good candidate for strengthening AFAs at elevated temperatures.

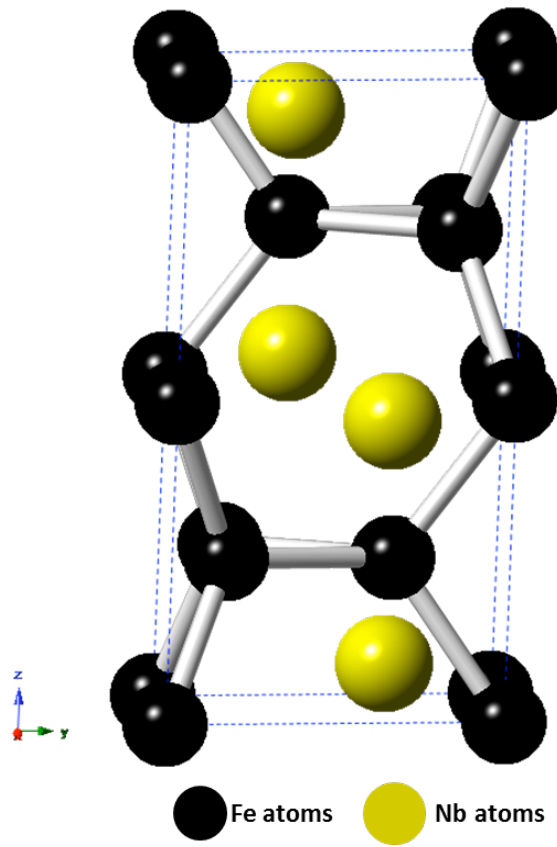


Figure 1.2: Diagram of the hexagonal C14  $\text{Fe}_2\text{Nb}$  Laves phase structure.

Prior work with the intermetallic Laves phase  $\text{Fe}_2\text{Nb}$  has shown that the strengthening effect of the precipitate is dependent on whether it precipitates on grain boundaries or in the austenitic matrix, and in what volume fractions and particle size it appears in the alloy<sup>20</sup>. See Figure 1.2 for a diagram depicting the hexagonal C14  $\text{Fe}_2\text{Nb}$  Laves phase structure. As the Laves phase particles increase in density and size, the brittle properties of the precipitate cause the material to lose its strength and creep resistance. Thus, a fine particle dispersion diameter of  $<100$  nm is recommended to match

the creep strength exhibited by AFAs strengthened with MC carbides and prevent failure of the material <sup>20</sup>. This decrease in the precipitate size and increase of the precipitate volume fraction in the austenitic matrix, allows for dislocations to be pinned leading to an increase in the alloy's creep strength. It has recently been shown by Tarigan et al. that in Fe-20Cr-30Ni-2Nb (at.%), the alloy's long-term creep resistance increased with an increasing area fraction of Laves phase precipitated on the grain boundary. It was also noted that dislocations that piled up near Laves phase grain boundaries were effective at suppressing local deformation by inhibiting the motion of dislocations and thereby increasing the long-term creep strength of the alloy <sup>42, 43</sup>. This creep-strengthening mechanism was coined "*grain boundary precipitation strengthening mechanism*" by Tarigan et al.

Yamamoto et al found that in addition to Fe<sub>2</sub>Nb Laves phase forming, after heat treating at 750°C, dense and fine B2-type NiAl precipitates formed in the  $\gamma$ -Fe matrix and on the grain boundaries <sup>21</sup>. The B2-type NiAl phase particles were dark in contrast and between 300 nm to 1  $\mu$ m in size. The Fe<sub>2</sub>Nb Laves phase particles appeared spherical with a bright contrast in the matrix and less than 500 nm in size. See Figure 1.3 for an example of precipitate contrast in Fe-20Cr-30Ni-2Nb-5Al (at. %). At elevated temperatures, B2-type NiAl precipitates play an important role in providing corrosion and oxidation resistance by acting as an aluminum reservoir for formation of the alumina protective layer <sup>44</sup>. They are not effective in improving the high-temperature tensile strength at temperatures greater than 400°C <sup>45,46</sup>, however it's been posited that B2-type

NiAl precipitates improve creep resistance by affecting the climb of dislocations in the matrix or the precipitate's resistance to dislocation slicing<sup>21</sup>.

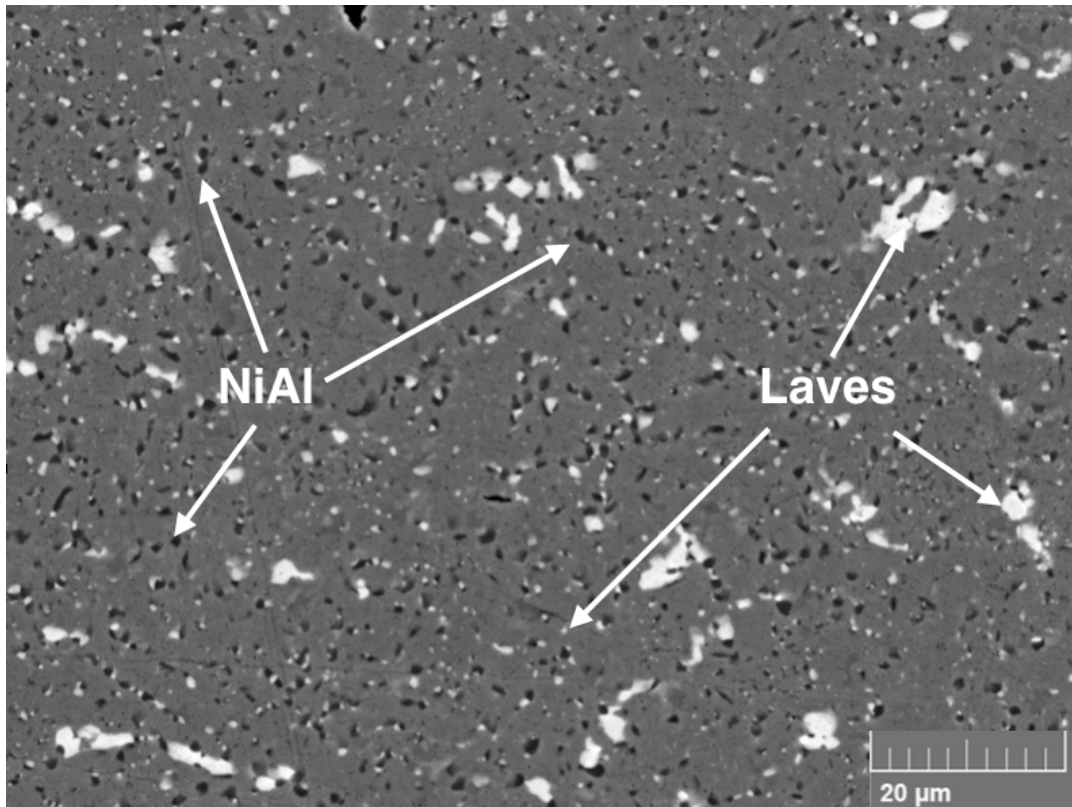


Figure 1.3: Backscattered electron images showing  $Fe_2Nb$  Laves phase (light contrast) and B2-type NiAl phase (dark contrast) precipitates in the matrix of Fe-20Cr-30Ni-2Nb-5Al (at. %) homogenized at 1250°C and heat-treated at 800°C for 240 h.

In order to better predict which precipitates are most beneficial for increasing AFA high temperature creep strength, further tests and characterization needs to be performed to form a better understanding of the complex interactions between the

presence of various precipitates and phases and their effect on the alloys' creep properties.

#### **1.4 Outline of Research Project**

The purpose of this thesis is to investigate the high-temperature strengthening mechanisms in alumina-forming austenitic stainless steels, specifically the high temperature constant-stress creep and mechanical properties of the model alloy Fe-20Cr-30Ni-2Nb-5Al (at. %) at different aging conditions.

The investigation proceeded as follows:

- 1) A constant-stress creep rig was designed, built and its operation validated
- 2) Samples were prepared from the model alloy and aged for time intervals of 0, 2.4, 24 or 240 h at 800°C
- 3) Constant-stress creep tests were conducted at elevated temperatures of 760°C
- 4) Secondary electron imaging was used to examine the microstructure of the samples prior to and after the completion of creep testing
- 5) Elevated temperature tensile tests were conducted on aged samples at 760°C

Chapter 2 focuses on the design, construction and testing of the constant-stress creep rig used in this investigation.

Chapter 3 covers materials preparation, testing procedures and materials characterization techniques.

Chapter 4 details the effect of aging time on the microstructural evolution and high temperature constant-stress creep and tensile behavior of the model alloy. The

observed microstructural changes and precipitate evolution prior to and after creep tests were conducted, are analyzed and discussed. Additionally, the observed differences of the mechanical properties of the alloy at different aging conditions is explored.

In Chapter 5 and 6, the conclusions of this research project are summarized and suggestions are made for future work.

## CHAPTER 2      CONSTANT-STRESS CREEP RIG DESIGN AND CALIBRATION

### 2.1      Introduction

This chapter details the design and calibration of a constant-stress creep rig constructed for use in this investigation to conduct high temperature constant-stress creep tests.

### 2.2      Overview of Constant-Stress Creep Machines

Creep testing machines take several forms depending on what is the primary target of investigation, which includes constant load, variable stress and constant-stress rigs. A small change in the level of stress can have a large effect on strain rate affecting both the overall creep rate and microstructure of the sample. With increasing strain, the cross-sectional area  $A$  of a test specimen decreases, which if tested in a constant-load creep rig, results in an increase in the instantaneous stress. With a load  $P$ , cross-sectional area  $A$ , the stress on the specimen will be  $\sigma = P/A$ . A constant-stress machine would allow the stress variable to be controlled by compensating for the decrease in the specimen's cross-sectional area by decreasing the effective load applied on the specimen. This allows the basic creep mechanisms acting on the specimens tested to be isolated and analyzed.

The curve of the constant-stress cam is key to constructing a precise, operational constant-stress creep rig. In Figure 2.1, a schematic layout of the weight-transferring system is shown for a constant-stress creep test applications. For constant-load creep tests, the curved cam would be circular.

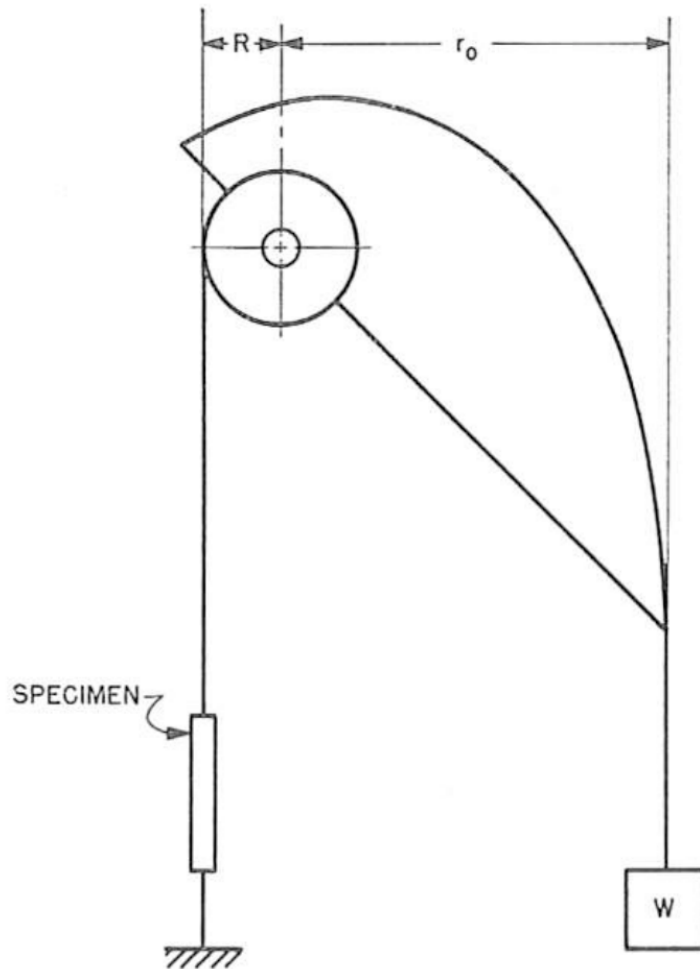


Figure 2.1: A schematic diagram detailing a weight-transferring system used for constant-stress creep tests.<sup>47</sup>

The curved profile of the constant-stress cam is analytically calculated using a system of parametric equations following the outline of an Andrade-Chalmers beam<sup>48</sup>. It is shown that the fixed Cartesian coordinates  $x$  and  $y$  of a constant-stress cam can be written in terms of constants and the angle  $\theta$  (see Appendix I for derivation of equations (1) and (2)), where  $\theta$  is the angle the cam makes with the horizontal as seen in Figure 2.2

from the paper by Garofalo et al (1962). In equations (1) and (2)  $L_0$  is the initial specimen gauge length prior to creep,  $r_0$  is the initial moment arm,  $R$  is the radius of the smaller load-transferring wheel. The Cartesian coordinates from which the profile of the cam can be traced for machining are determined by the values of constants  $a$  and  $b$ :

$$a = \frac{r_0 L_0}{L_0 - R\theta_0} \quad \text{and} \quad b = \frac{R}{L_0 - R\theta_0}$$

$$x = \frac{a}{1 + b\theta} \left[ \cos(\theta) + \frac{b \sin(\theta)}{1 + b\theta} \right] \quad (1)$$

$$y = \frac{a}{1 + b\theta} \left[ \sin(\theta) - \frac{b \cos(\theta)}{1 + b\theta} \right] \quad (2)$$

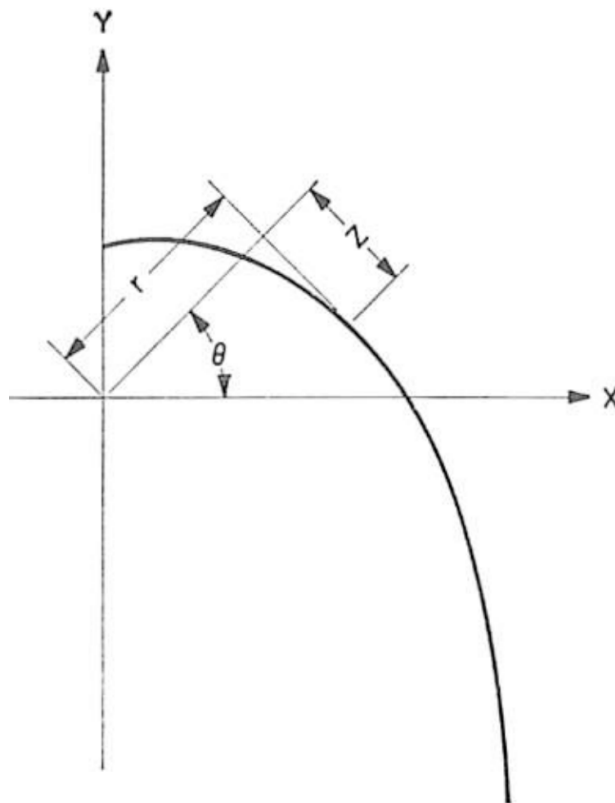
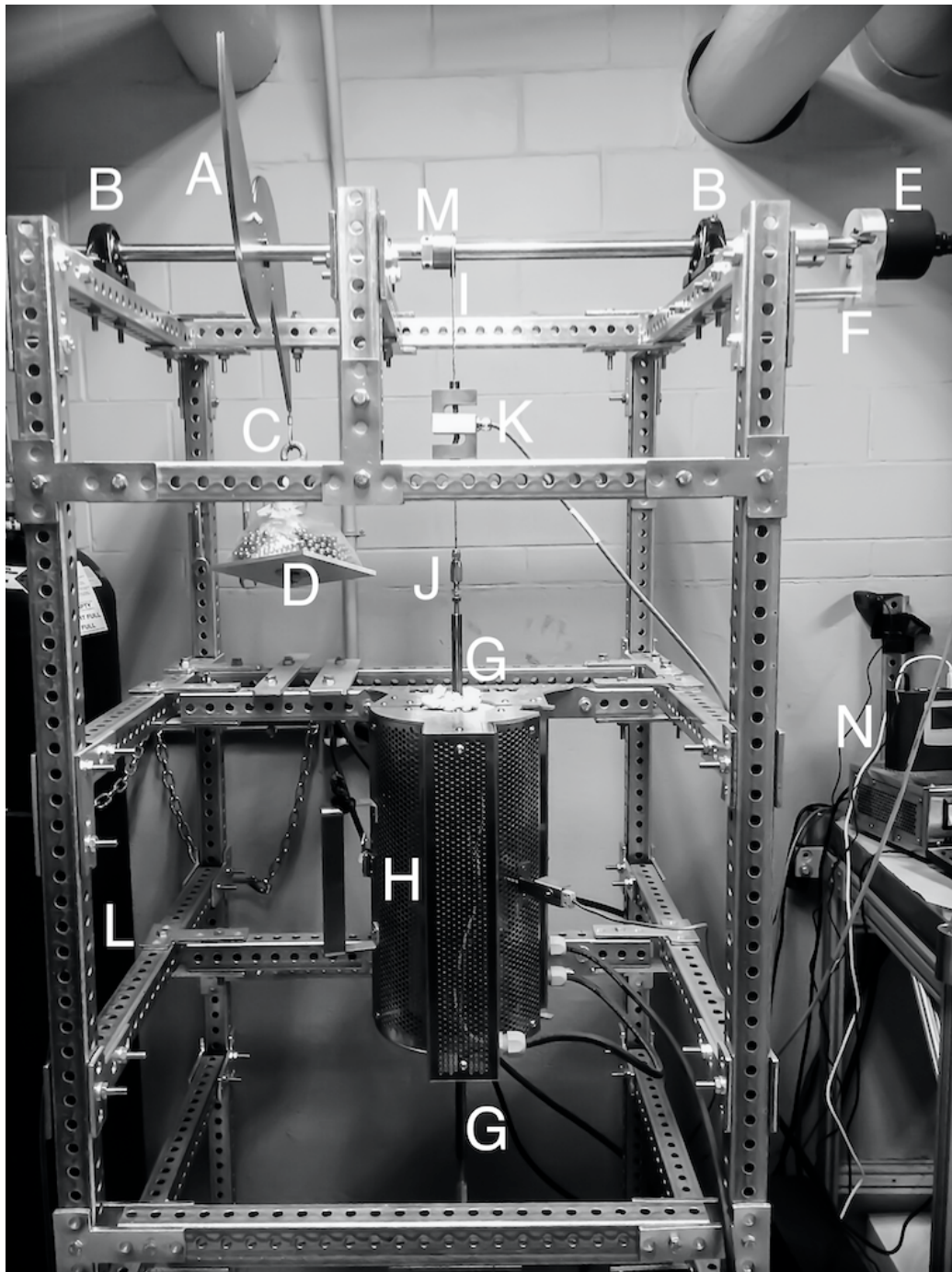


Figure 2.2: A diagram detailing the coordinate system used for the cam profile

For the purposes of this investigation, a constant-stress creep test rig was custom-designed, built and its operation validated based on the methods developed by Garofalo, Richmond and Domis (1962). The following section discusses the system's dimensions, assembly, cam parameters, calibration and testing procedure.

### **2.3 Design of Creep Test Rig**

A photograph of the full assembly of the creep rig is shown in Figure 2.3 with a sample specimen in tension and placed under a 35 MPa load.



*Figure 2.3: Photograph of the constant-stress creep machine with system components labeled matching the key*

Key for Figure 2.3

- A. Constant-stress cam
- B. Bearing pillow block
- C. Cable attached to load
- D. Load weight on loading tray
- E. Angular Displacement Transducer (ADT)
- F. ADT support
- G. Connecting rod
- H. Mellen Furnace
- I. Cable attached to specimen
- J. Swageless Thread Terminal
- K. Linear variable differential transformer (LVDT)
- L. Steel Frame
- M. Load-transferring wheel
- N. Data Logger

\* Letters in parentheses () indicate machine components as per Figure 2.3

### 2.3.1 *Frame and Mounts*

The metal frame (L) of the rig is made of 1.5-in galvanized steel perforated tubing for heavy duty telescoping framing and is bolted onto four base mounts to account for uneven floor surfaces. The metal frame additionally supports the Mellen Inc. SCR Split Series 120 V 1200 W Furnace (H) mounted vertically. The furnace utilizes clamshell-heating elements capable of 1250°C in air. The temperature is measured with a centrally located K-type thermocouple and controlled by a Mellen Inc. PS105 programmable power control cabinet. Two heavy-duty ball bearing pillow blocks (B) are rigidly attached to the steel frame and support a 0.75-in diameter steel rod that acts as the cam and load-transferring wheel support shaft.

### 2.3.2 *Constant-Stress Cam*

As discussed in the previous section, the cam profile is dictated by the constants  $a$  and  $b$ . For a small load-transferring wheel with a radius of 0.75 inches, an initial specimen gauge length of 0.787 inches and a desired mechanical advantage of 8:1, the values of  $a = 6.00$  in and  $b = 0.95$  in. Using the derived equations (1) and (2) and the calculated values of  $a$  and  $b$ , the Cartesian coordinates of the cam's profile in  $x$  and  $y$  can be calculated for a given angle  $\theta$  as shown in Table 2.1.

Table 2.1 Coordinates for the constant-stress cam profile fabricated for use in this study, with  $a = 6.00$  in and  $b = 0.95$  in.

$\Theta$ (deg)	x (in)	y (in)
-20	4.06	-15.13
-15	5.10	-11.87
-10	5.66	-9.35
-5	5.93	-7.34
0	6.00	-5.72
5	5.94	-4.37
10	5.80	-3.24
15	5.59	-2.29
20	5.33	-1.48
25	5.05	-0.79
30	4.74	-0.20
35	4.42	0.30
40	4.09	0.74
45	3.75	1.10
50	3.41	1.41
55	3.08	1.67
60	2.74	1.89
65	2.42	2.06
70	2.10	2.19
75	1.78	2.29
80	1.48	2.35
85	1.19	2.39
90	0.92	2.40
95	0.65	2.39
100	0.40	2.36
105	0.17	2.31
110	-0.05	2.24
115	-0.26	2.15
120	-0.45	2.05
125	-0.62	1.94
130	-0.78	1.82
135	-0.92	1.69
140	-1.05	1.55
145	-1.16	1.41
150	-1.25	1.26
155	-1.33	1.11

The constant-stress cam (A) and the load-transferring wheel (M) are mounted on the steel rod with a diametrical interference fit of 0.003-in, which facilitates free circular movement around the rod. The cam profile shown in Figure 2.1 is duplicated, inverted and attached to the original cam profile to balance the cam assembly when it's threaded onto the support rod. The small radius load-transferring wheel is designed for an 8:1 mechanical advantage. Both the cam and the wheel are attached to the center support shaft with a collet and two set screws placed on opposing sides and screwed in to firmly secure the components and eliminate movement when the system is under load. The cam and the load-transferring wheel are fabricated from 1018 steel. Appendix II contains CAD drawings with specifications of the cam and load-transferring wheel.

### *2.3.3 Angular Displacement Transducer*

The TransTek Inc. Series 600 Model 0603-0000 Angular Displacement Transducer (ADT) with 100 mV/ $^{\circ}$  output and maximum usable range of  $\pm 40^{\circ}$  is attached (E) with a set screw to the end of the support shaft extending 1 inch past the pillow block and steel frame tubing. The ADT allows for measuring specimen elongation by tracking the angular displacement of the cam shaft as the sample lengthens throughout the duration of a creep test. More specifically, as the specimen creeps, the relative displacement of the two specimen grips is detected by the ADT. This angular displacement is translated into an electrical signal, which is then amplified by the TransTek Inc. Series D100 Dual DC 12VDC Power Supply and sent by the readout wire to the Grant Instruments Ltd. SQ2010 Portable Universal Input Squirrel

Data Logger (N) to monitor, measure and record the elongation of the specimen. The high accuracy ADT is capable of measuring an angular displacement of  $\pm 0.10\%$ , which translates to measuring a linear displacement of  $<0.001$  in. The ADT is supported with an aluminum bolted frame (F) to eliminate any torque placed on the high-precision measurement equipment.

#### *2.3.4 Cable and Load Alignment*

Both the constant-stress cam and the load-transferring wheel have a 0.047-in radius milled groove on their outlines to create a track that allows for a 3/32-in wire cable to fit and wrap around with a snug fit. A wire 3/32-in cable (C) is attached to the constant-stress cam through a pinhole, shown in Figure 2.4, and swaged together with wire rope sleeves. The other end of the cable is swaged in the form of a loop and permits the attachment of a dead-weight load. The load is attached through the use of an 8-inch long metal hook threaded through the center of an aluminum 6x6-in square platform (D). The load is stacked on the platform. The material used for the applied load consists of steel 1/4-in diameter balls to aid in applying a variety of loads with precision.

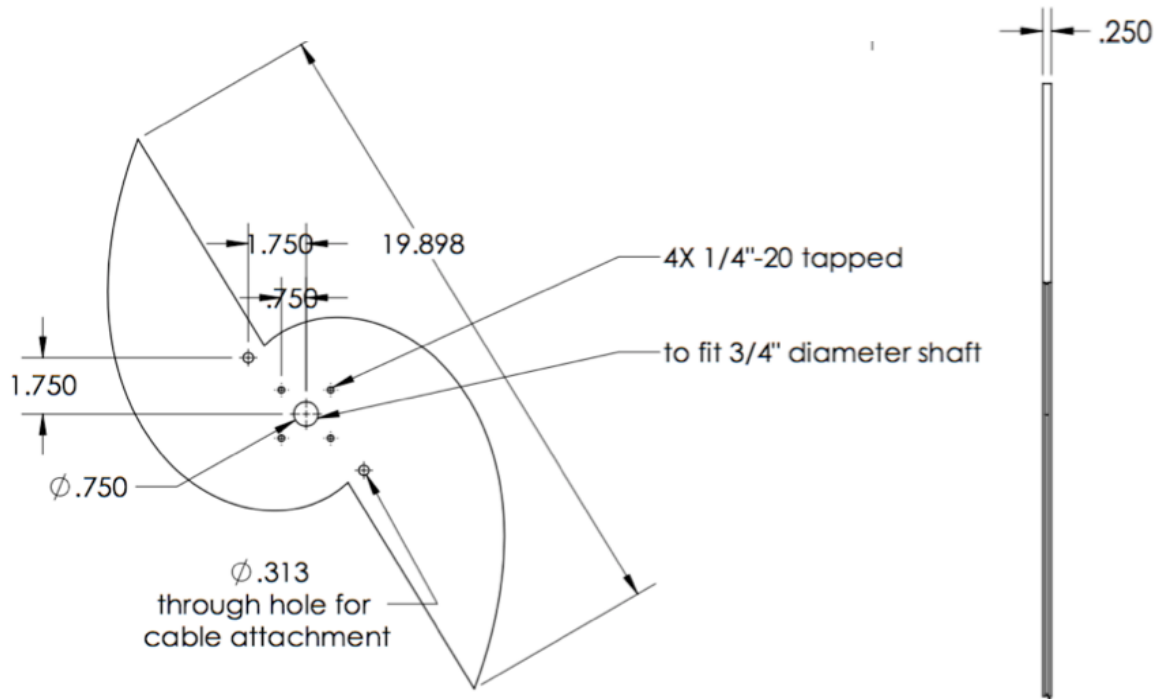
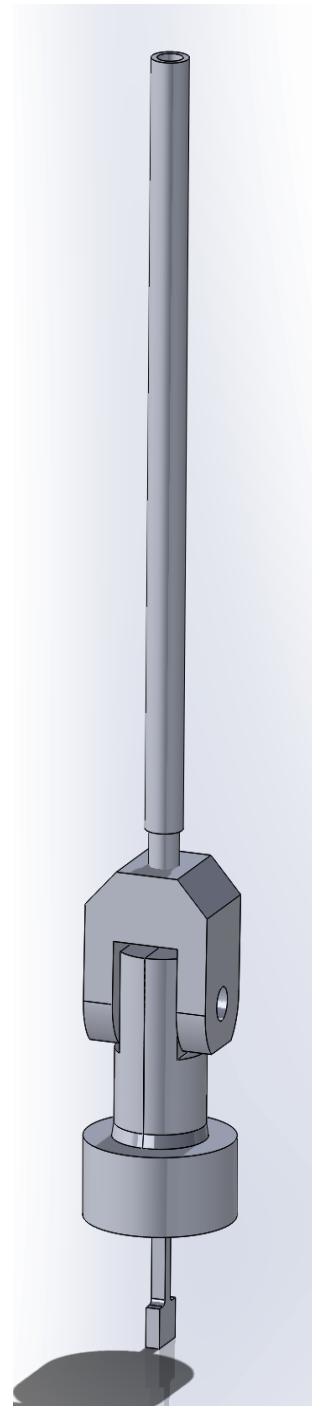


Figure 2.4: Design drawing of constant-stress cam

One end of a wire 3/32-in cable (I) is attached and swaged through a pinhole to the load-transferring wheel (M) on the opposite side that the cable is attached to the constant-stress cam. The other end of the cable drops vertically down to connect through two attachment openings in the vertically aligned Omega Engineering Inc. LC101-500: 500 lb S-beam load cell (K), which acts as the linear variable differential transformer (LVDT). The LVDT output wires are connected to the data logger (N) and Omega Engineering Inc. DP25B-S-A series Digital Panel Meter with a 4-digit LED display that aids in adjusting the cam placement when a load is applied by displaying the output in lbf units. A wire cable is attached through the bottom of the LVDT to a swageless thread terminal (J).

### 2.3.5 *Specimen Grip Components*

The thread terminal is screwed into the machined upper extension connecting rod (G). The extension rod is screwed into the upper male end of the machined specimen grips as shown in Figure 2.5. The specimen grips and connecting rods are fabricated from 718 Inconel to prevent elongation when heated in the furnace, and hold the specimen in a vertically aligned position. The lower specimen grips are similarly connected to an extension rod, a swageless thread terminal and a wire cable. Figure 2.5 shows a diagram of the details of the specimen grips. Appendix II contains CAD design drawings of the grip components, which includes the inner grips, collets, yolks, and rod connectors.



*Figure 2.5: Diagram of specimen grips*

### *2.3.6 Making Adjustments*

Completing the linkage, the wire cable is vertically secured to the bottom crossbeam of the steel frame in a 1/4-in diameter slot to allow for lateral movement and adjustments of up to 2 inches when a load is applied to the system and the cable is placed under tension.

Of special note is the horizontal position mark that is inscribed on the constant-stress cam prior to the system assembly. The cam is designed to produce a constant-stress about this centerline as shown in Figure 2.6, which aids in proper adjusting and positioning of the cam during calibration testing such that the rig functions as intended (refer to Calibration Testing section 2.4.4).

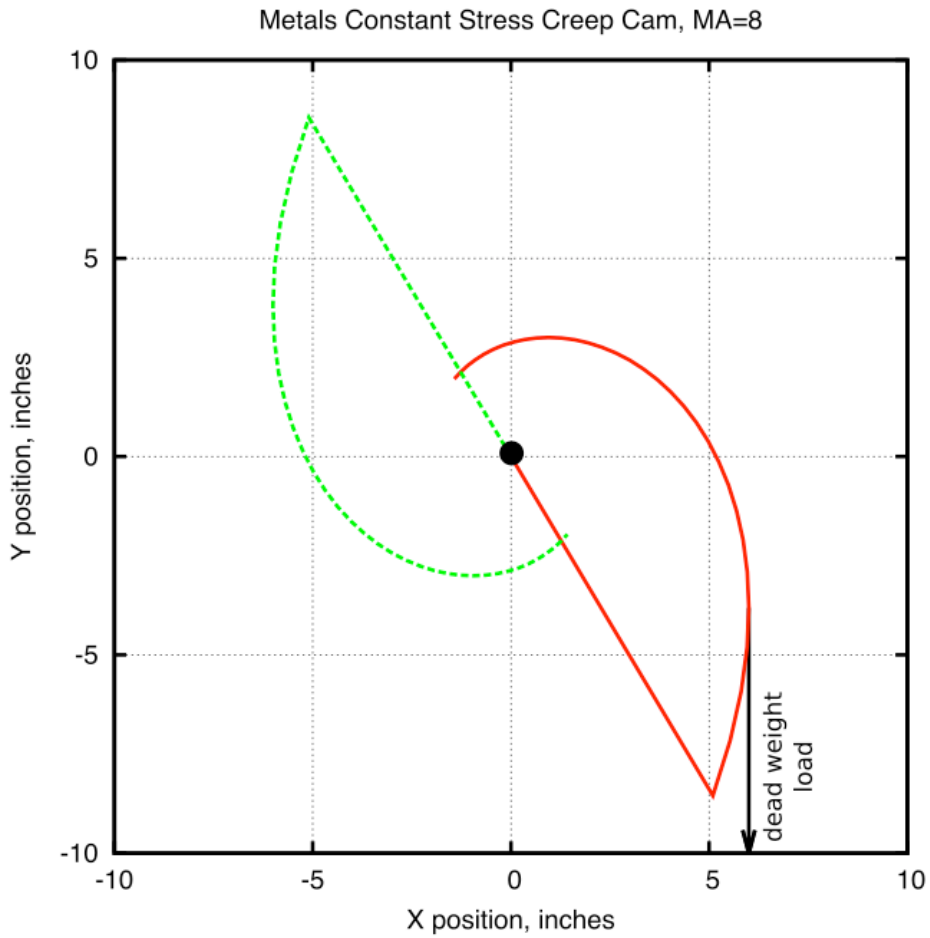


*Figure 2.6: Plot of the constant-stress cam geometry. The cam's centerline is centered on  $y = 0$ .*

### 2.3.7 Data Logging

The Squirrel data logger receives amplified voltage readouts from the ADT and LVDT. The output is sampled at five-second intervals and then logged as an average of five samples. This logging rate allows for long term creep tests to be conducted by decreasing the amount of data logger memory used, while ensuring the data collected has appropriate resolution for detailed data analysis.

## 2.4 Testing and Verification

A range of tests were performed on the creep rig to verify that the system functioned as intended. The machine was calibrated for use with a load of 35 MPa, and a series of tests were conducted to prove that the load on the test sample would be reduced at the specified rate to produce a constant-stress.

### 2.4.1 Identifying the ADT Adjustment Factor

The Angular Displacement Transducer (ADT) output is a voltage, which is converted to an angular displacement in degrees. This rotational displacement value is used to calculate the elongation of the test specimen to a high degree of precision. The ADT displacement measurements required an adjustment factor to match the actual test specimen elongation.

To conduct the test and acquire the adjustment factor, a sample test specimen was placed in the system and the effective load was decreased in 5 MPa increments by mechanically simulating a displacement of the specimen, which was accomplished by unscrewing the upper connecting rod out of the upper specimen grip connector. The data logger was used to record the angular displacement recorded by the ADT, and a micrometer was used to measure and record the simulated linear displacement. The test was conducted three times and the data was averaged. Figure 2.7 shows the results of this calibration.

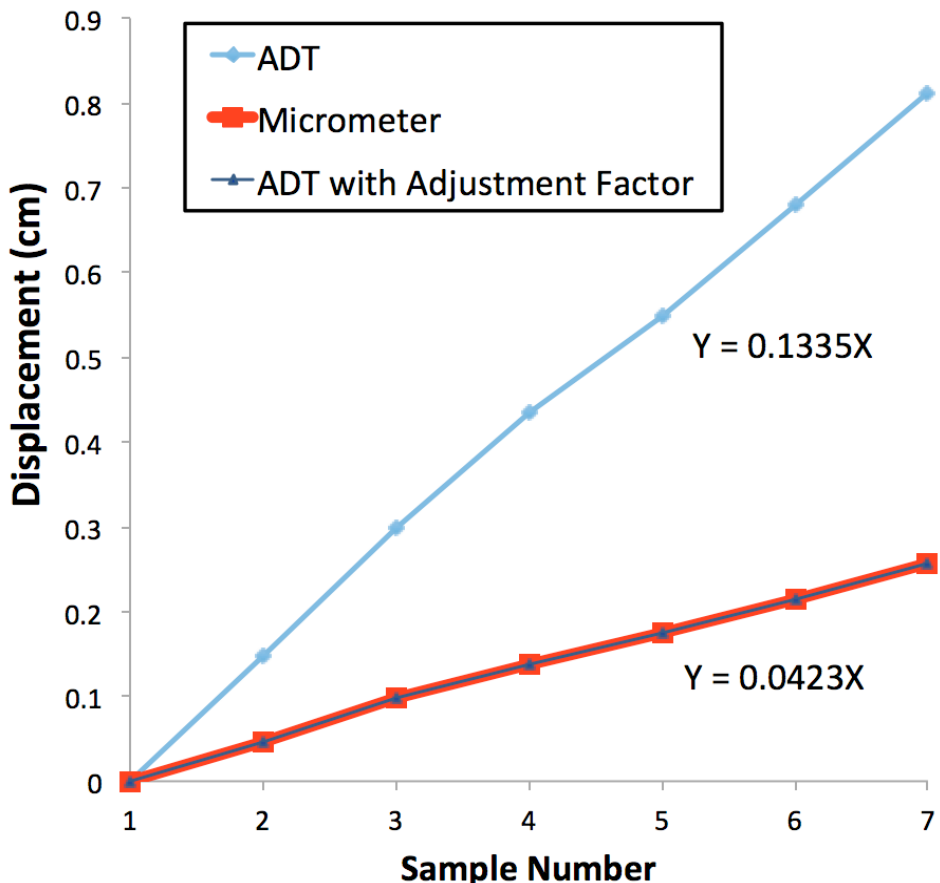


Figure 2.7: Plot of system displacement measurements taken with ADT, manually with a micrometer and the same ADT results plotted with an adjustment factor. Notice the adjusted ADT measurements match those taken with the micrometer.

When the ADT results were adjusted with a factor of 3.156, the displacement values were identical to those taken with the micrometer. This verified that the system recording displacement accurately measured and recorded specimen elongation.

#### *2.4.2 Eliminating Creep Contributions From System Components*

A test was performed to determine if the connecting components of the system, such as the connecting rods, cable and grips, would creep under an applied load and affect the test results by contributing to the overall creep measured.

A sample T-bone was fabricated from 718 Inconel and heat treated, which is the same material from which the specimen grips and connecting rods were fabricated. The sample was inserted into the specimen grips and the system put under a load of 35 MPa (the load used for subsequent testing in this investigation). The system was tested for a 24 h duration. An initial displacement was recorded by the ADT within the first few seconds of the system coming under load, which can be attributed to the elimination of slack in the system.

No creep of the system components was detected for the duration of the 24 h period. This demonstrated that the only contributing factor to subsequent tests' resulting creep was attributed to elongation of the T-bone specimens and not to the creep of components of the system.

#### *2.4.3 Furnace Temperature Profile*

The furnace to heat the sample at a constant temperature was vertically aligned and therefore its temperature profile was measured to ensure that the temperature felt by the test specimen was indeed the temperature set point being measured by the K-type thermocouple in the furnace.

A second thermocouple was inserted along the inside length of the furnace and used to identify the location at which the measured temperature matched that being displayed as the set point on the furnace power control cabinet. This test was repeated three times and the results averaged with a final location determined to be 5.5 inches measured from the top of the furnace tube or 6.5 inches measured from the tube bottom exit. The system cables were adjusted accordingly to ensure that when under load, the test specimen would be located at the target height.

#### *2.4.4 Calibration Testing*

For a constant-stress test, the equation:

$$P/P_0 = L_0/L \quad (1)$$

where  $P$  is the load and  $L$  is the length of the specimen, must be satisfied for any angle and for any initial load  $P_0$  in order to satisfy the requirement that  $PL = \text{constant}$ . The creep rig was calibrated by comparing the theoretical predictions of equation (1) with experimental measurements of  $P$  and  $L$ .

Before beginning the calibration test, the cam was adjusted so the horizontal position mark inscribed on its side was level and at the intended zero mark. The furnace door was propped open to expose the specimen grips inside and a test specimen inserted. Steel balls with a total load 45 MPa were placed onto the loading tray. A zero reading was taken and recorded. The angle was increased in 5-degree increments, by mechanically simulating a displacement of the specimen, from 0 to 35 deg. For each interval, the load and linear displacement were recorded.

Figure 2.8 shows the calibration plot. The experimental values had an average variation of 0.36 percent compared to the theoretically predicted values from equation (1). This value was well within the bounds of literature values<sup>47</sup> confirming the rig was calibrated and operational for constant-stress testing.

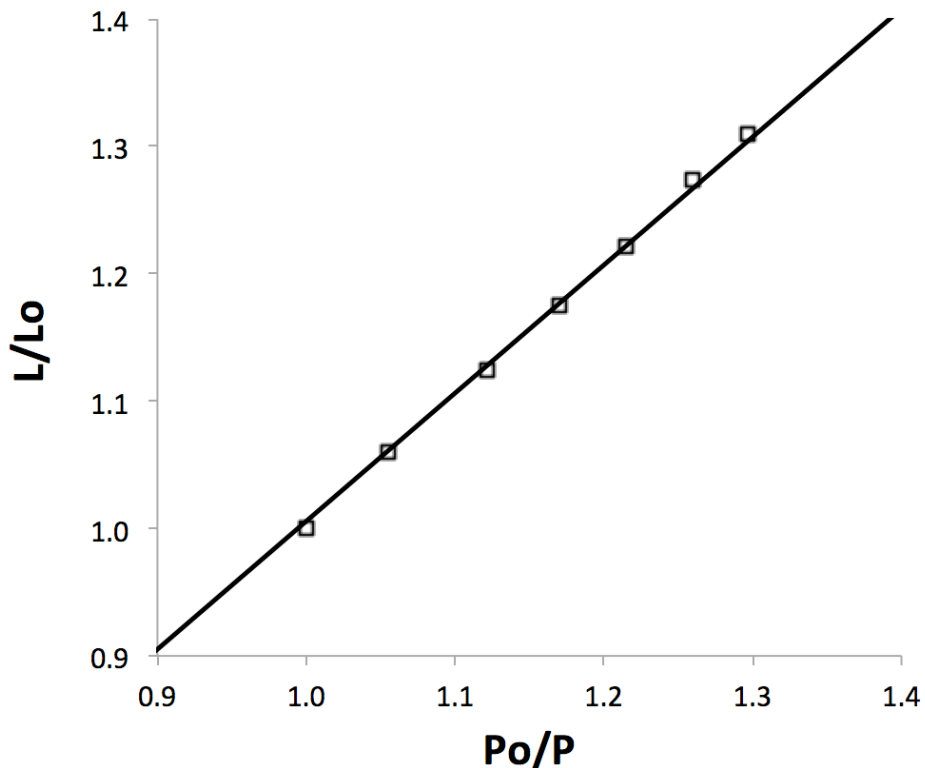


Figure 2.8: Load calibration of constant-stress cam

## CHAPTER 3      EXPERIMENTAL METHODS

### 3.1      Introduction

This chapter details materials preparation and processing methods, constant-stress creep testing procedures, tensile testing and materials characterization techniques involved in this work.

### 3.2      Materials Preparation

#### 3.2.1    *Materials Used*

The alloy Fe-20Cr-30Ni-2Nb-5Al (at.%) was used for both the creep and strain-rate jump tests throughout this study. The alloy was provided by Mr. Michael Schmidt, Carpenter Technology Corporation (Wyomissing, PA). A split-cast vacuum induction melting heat was used to cast the alloy into 8 kg tapered ingots. The ingots were then press forged into rectangular bars with the following dimensions: 0.625" x 0.75" x 24". The chemical composition of the alloy was analyzed by LECO combustion analysis and X-ray Fluorescence. Table 2.1 compares the analyzed element compositions with the theoretically calculated weight percent ratios, demonstrating agreement between the predicted and actual chemical composition of the cast alloy.

*Table 3.1 Alloy compositions obtained by chemical quantitative analyses*

<b>Element Analyzed</b>	<b>Theoretical (wt%)</b>	<b>Analyzed (wt%)</b>
Nickel	31.88	31.9
Chromium	18.83	18.98
Niobium	3.36	3.34
Aluminum	2.44	2.48
Carbon	0.00	0.02
Cobalt	0.00	0.01
Copper	0.00	<0.01
Manganese	0.00	<0.01
Molybdenum	0.00	0.01
Phosphorus	0.00	<0.005
Silicon	0.00	<0.01
Sulfur	0.00	<0.001

### 3.2.2 Sample Machining

In preparation for both creep testing and strain-rate jump tests, the alloyed material was machine milled and then sectioned with a saw. The TRAK DPM SX3P bed mill with a 40 taper spindle and ProtoTRAK SMX control was used with zinc-coated carbide end mills to mill the specimens into the T-bone shapes necessary to insert into the specimen grips of the creep testing and strain-rate jump testing machines as shown in Figure 3.1. To ensure the accurate geometry of each T-bone, the specimen was sectioned using coolant with a Model 650 Low Speed Diamond Wheel Saw from South Bay Technology, Inc.

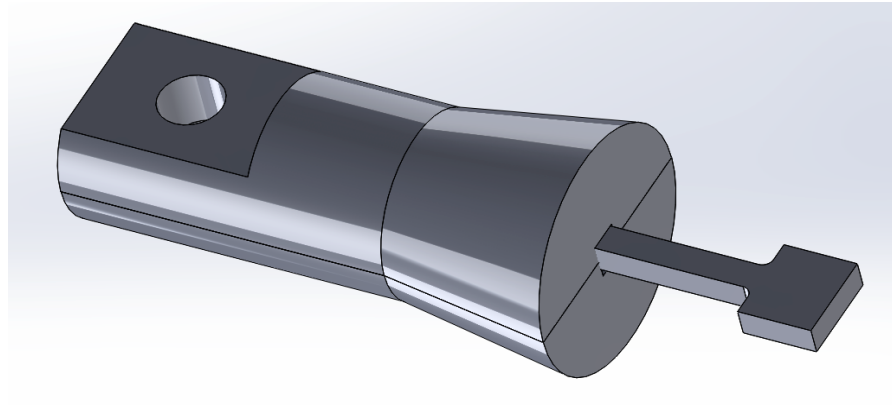


*Figure 3.1: CAD file drawing of a T-bone specimen inserted into one side of the creep machine's specimen grips.*

### *3.2.3 Material Homogenization*

Solutionizing anneals were necessary to homogenize the material for a uniform microstructure. For all tests in this study, the as-cast model alloy was homogenized for 24 h at 1250°C in a vacuum and then water-quenched. This temperature and time was chosen with consideration to prior work with Fe-20Cr-30Ni-2Nb-5Al, where it was determined that a solutionized single phase  $\gamma$ -matrix could be consistently formed. This was confirmed with SEM images of the as-cast raw material and compared with the material after a heat treatment homogenization conducted at 1250°C for 24 h.

All solutionizing heat treatments were conducted using a Thermo Scientific Type 54233 Lindberg Closed-Shell tube furnace. Specimens were placed on top of a piece of alumina and maneuvered to the center of the furnace tube with a rod. The furnace tube was then purged with argon and placed under a pressure of 0.01 MPa to maintain an oxygen-free environment and to prevent oxidation of the sample inside the furnace until

the heat treatment was complete. Once the sample was sealed inside the furnace, the furnace was turned on and the temperature set to 1250°C. When the solutionizing anneal was complete, the pressure seal was broken and the sample rapidly quenched in water with a substantially greater mass compared to the sample.

#### 3.2.4 *Annealing*

All heat treatments of the samples after they were homogenized were conducted at 800°C for a variety of time intervals of 0, 2.4, 24 or 240 h. Heat treatments were conducted in a Barnstead Thermolyne Type 47900 Furnace. Samples were placed inside an alumina crucible and then positioned at the center of the furnace for the duration of the heat treatment. At the completion of the heat treatment, the samples were quenched with water.

### 3.3 Materials Characterization

#### 3.3.1 *Scanning Electron Microscopy*

In preparation for imaging with the scanning electron microscope (SEM), samples were compression mounted and polished on a turntable using successively finer silicon carbide abrasive paper up to 1200-grit, then with 0.3  $\mu\text{m}$  followed by a finer 0.05  $\mu\text{m}$  alumina powder dissolved in water. Samples were placed on a polishing vibrometer with a thin layer of diluted MasterMet Colloidal Silica Polishing Suspension solution for ~3 h to eliminate surface defects and achieve a mirror finish. After the polishing was complete, the samples were washed with a spray of distilled water, then methanol,

followed by a light scrubbing with a cotton swab and detergent to eliminate any adhered alumina particles.

Samples were imaged using a Tescan Vega3 SEM outfitted with Bruker Quantax Energy-dispersive X-ray Spectroscopy (EDS) and electron backscatter diffraction (EBSD) detectors. Samples were imaged using back-scattered electrons (BSE) with a working distance of 10 mm and operating voltage of 15 keV. To distinguish the matrix, NiAl and Laves phase precipitates, BSE images were used for microstructural analysis due to BSE differentiating based on atomic number.

### *3.3.2 Transmission Electron Microscopy*

For thin-film TEM examination, material was prepared by sectioning discs from samples that were milled into the form of 3 mm diameter cylindrical rods. The specimens were ground and mechanically polished to a thickness of ~0.2 mm. They were electrolytically thinned in a polishing electrolyte solution consisting of 20% nitric acid and 10 % butoxyethanol in methanol in the temperature range of -20 to -25°C using the Struers TenuPol-5 apparatus with a voltage of 10 V and current of ~50 mA. After being electropolished, the samples were rinsed three times with ethanol.

The resulting samples were placed in a double-tilt holder with a capability of tilting 60° along two axes in order to adjust the specimen orientation during analysis. TEM investigations to characterize the microstructure of the material were performed using a Philips Tecnai F20 FEG-TEM under an accelerating voltage of 200 kV.

### 3.4 Constant-Stress Creep Testing

#### 3.4.1 Sample Preparation

Following verification and calibration of the creep rig as described in section 2.4 of Chapter 2, creep test specimens were milled from the Fe-20Cr-30Ni-2Nb-5Al (at. %) model alloy to a 3 mm thickness, with a gauge length of 20 mm, width of 3mm and overall length of 35 mm as detailed in Figure 3.2. Each specimen was homogenized for 24 h at 1250°C to produce a single phase material. Specimens were subsequently aged in air at 800°C for 0, 2.4, 24 or 240 h.

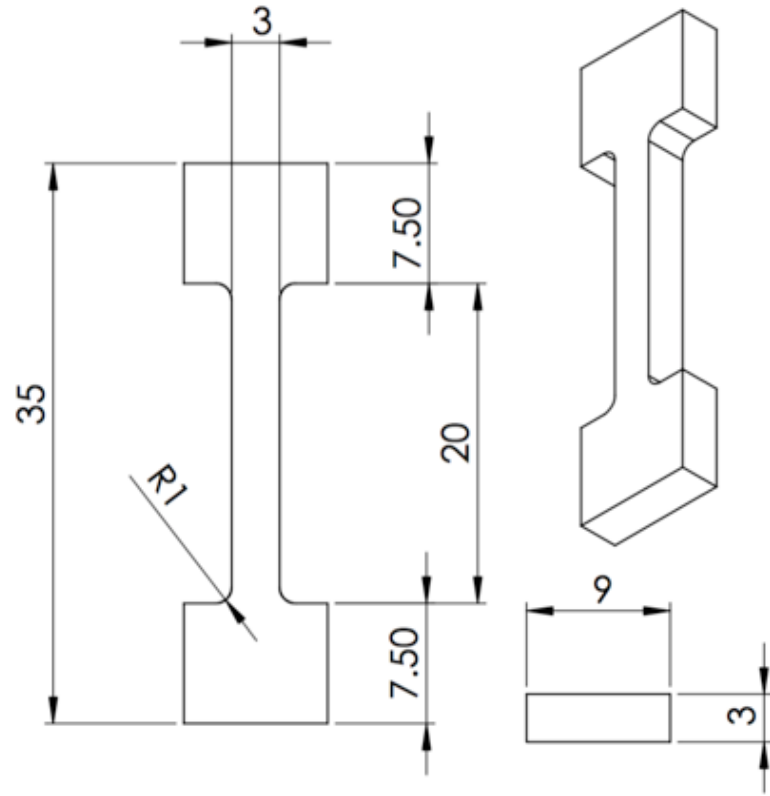


Figure 3.2: Dimensions of creep test specimen in millimeters.

Prior to conducting creep tests, one representative sample from each heat treatment procedure was mounted, polished and imaged using the SEM as detailed in section 3.3.1. These imaged samples provided a baseline for each heat treatment to compare to the specimen microstructures after they had undergone a creep test.

### *3.4.2 Creep Test Experimental Procedure*

Test specimens were inserted into the high temperature specimen grips and the furnace door locked. Glass wool was placed over the top and bottom furnace openings to reduce air currents and increase temperature uniformity throughout the furnace. 4.015 kg were placed on the loading tray for a total load of 35 MPa, but not attached to the cam cable wire attachment loop. The cam was set so that the inscribed horizontal position mark was level and the furnace set to 760°C. This temperature was chosen for all creep tests, because it matches the target application temperature for AFA stainless steels. Upon reaching the desired temperature, the weighted loading tray was hooked on the wire cable attachment loop and the system put into tension. When the loading tray stabilized within a few seconds, the data record button on the data logger would be pressed to begin data logging. Temperature was held constant in each test.

At 760°C and under a 35 MPa load, it was established that the model alloy tested would enter the secondary creep regime approximately one hour after the specimen was put into tension by loading. It would remain at a steady state for at least a 1000 h duration (the longest duration tested). To capture a representative sample of the creep curve, the

duration of each test was 500 h, with the exception of two shorter partial tests conducted to evaluate microstructural changes at stages on the creep curve.

Upon completion of a test, data recording would be terminated, the system unloaded and the furnace ramped down to room temperature. The test specimen would then be removed from the specimen grips and sectioned into three parts using a diamond saw as described in section 3.2.2. Figure 3.3 shows the locations of where the head, gauge and gauge-lengthwise sections were located along the T-bone specimens. These three locations were chosen to explore any differences in precipitate directionality or observable microstructural differences between the three section.

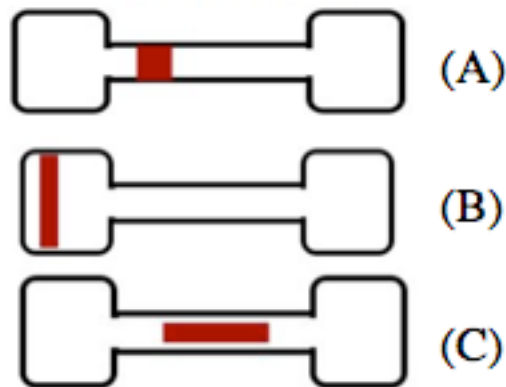


*Figure 3.3: Diagram detailing the locations of sections taken for SEM microstructural analysis from crept T-bones. (A) Gauge (B) Head (C) Gauge-lengthwise*

Creep curves of strain percent over time were produced from the load and displacement data collected. Each crept sample was mounted, polished and imaged using scanning electron microscopy as detailed in section 3.3.1.

### 3.4.2 Creep Test Experiments Performed

Elevated temperature constant-stress creep tests were conducted for a duration of 500 h for each aging condition at 760°C under a 35 MPa load. Each 500 h test was completed twice for each aging condition. Two partial constant-stress creep tests were conducted to evaluate the alloy's microstructural changes as it crept over time. Similar test conditions as the full range 500 h creep tests were used for the partial tests. Two specimens were homogenized at 1250°C but not aged. The first test was run for 3.5 h and the second test was stopped after a 300 h duration to get representative samples along the creep curve. Samples were mounted, polished and imaged on the SEM after the creep tests were complete and creep curves of strain percent over time were produced from the load and displacement data collected.

## 3.5 Tensile Tests

Flat T-bone test specimens approximately 1 mm thick, with a gauge length of 15 mm, and width of 2 mm were milled with the dimensions shown in Figure 3.4 from the Fe-20Cr-30Ni-2Nb-5Al model alloy as detailed in the materials preparation section 3.2.2. Each specimen was homogenized at 1250°C for 24 h and then aged at 760°C for 0, 2.4, 24 or 240 h. Specimens were polished on a turntable using successively finer silicon carbide abrasive paper up to 1200-grit, then with 0.3  $\mu\text{m}$  alumina powder dissolved in water.

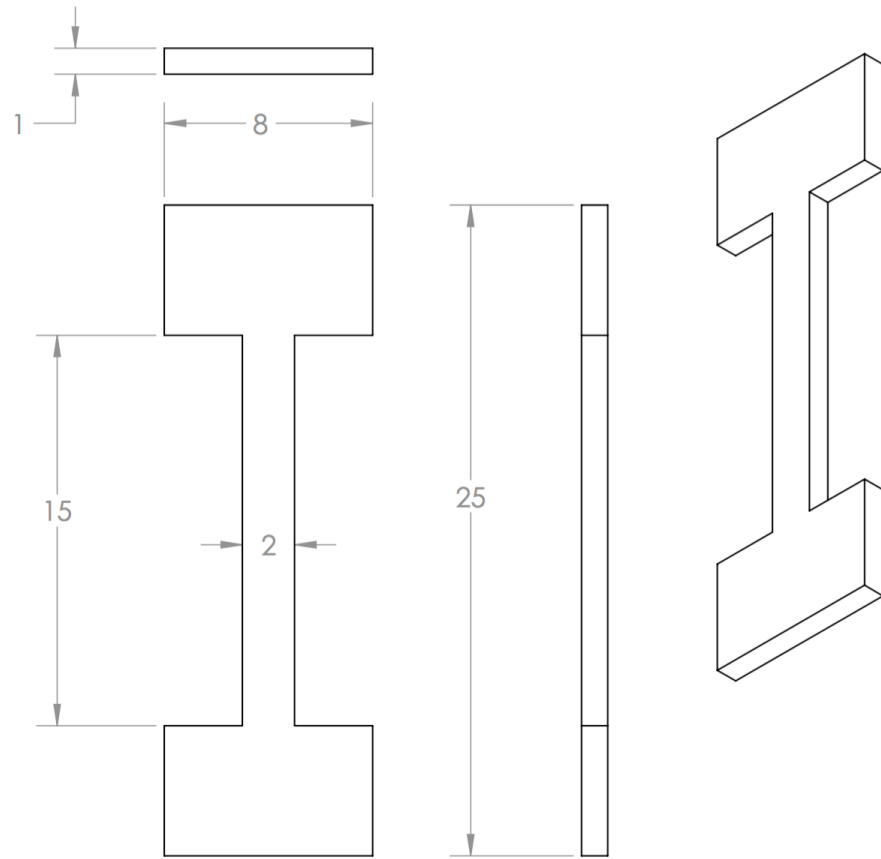


*Figure 3.4: Dimensions of tensile test specimen in millimeters.*

Samples were inserted into high-temperature specimen grips of the Instron 5690 tensile testing machine coupled with a MTS hydraulic testing machine. The metal frame of the Instron supports the Mellen Inc. SCR Split Series 120 V 1200 W Furnace mounted vertically. The furnace utilizes clamshell-heating elements capable of 1250°C in air. The temperature was measured with a centrally located K-type thermocouple and controlled by a Mellen Inc. PS105 programmable power control cabinet.

Elevated temperature tensile tests were conducted at 760°C with an applied preload force of 50 N. For all tests the initial strain rate was  $5 \times 10^{-4} \text{ s}^{-1}$ , and up to five

tensile tests were performed for each heat treatment protocol. To decrease the number of repeat tests that had to be performed, a soft mallet was used to secure the T-bones in the high temperature grips.

True strain ( $\epsilon$ ) and true stress ( $\sigma$ ) were calculated from the load-displacement data and reported as true stress-strain curves. The yield strengths and ultimate tensile strengths were recorded. Percent elongation of the specimen was obtained by comparing the initial specimen gauge length and measuring the specimen gauge length after the tests were complete in an optical microscope. To examine the fracture surface, samples were prepared and imaged using scanning electron microscopy as detailed in section 3.3.1.

# **CHAPTER 4        EFFECT OF AGING TIME ON**

## **MICROSTRUCTURE AND HIGH TEMPERATURE TENSILE AND**

## **CONSTANT-STRESS CREEP BEHAVIOR OF THE ALUMINA-**

## **FORMING AUSTENITIC STAINLESS STEEL Fe-20Cr-30Ni-2Nb-5Al**

### **4.1     Introduction**

In this chapter, the effects of aging time on the microstructure and high temperature creep and tensile behavior of the alumina-forming austenitic stainless steel model alloy Fe-20Cr-30Ni-2Nb-5Al (at.%) is investigated. High temperature tensile tests were performed and compared to room temperature results. Constant-stress creep tests were performed at an elevated temperature and the microstructure analyzed before and after each creep test. Additionally, the effect of aging temperature on the presence of precipitates in the alloy's matrix was explored.

### **4.2     Experimental**

Bright-field TEM was used to investigate the effect of aging temperature on the presence of precipitates in the alloy's matrix, specifically on the presence of  $\gamma'$ -Ni<sub>3</sub>Al (L<sub>1</sub><sub>2</sub>) at 760°C as detailed in Chapter 3.

To explore the effects of aging time on the microstructure of the alloy, specimens were homogenized at 1250°C and then aged 0, 2.4, 24 or 240 h at 800°C. Microstructural analysis, namely focused on Laves phase and NiAl precipitates, was performed on the specimens for each aging condition using images taken by the SEM. To distinguish the

matrix and the precipitates, BSE images were used for the microstructural analysis due to BSE differentiating based on atomic number.

The area fraction of grain boundary Laves phase and NiAl precipitates (designated as  $\rho$ ) for Fe-20Cr-30Ni-2Nb-5Al (at. %) was quantitatively analyzed using equation (1)<sup>49</sup>, where  $l$  is the length of the grain boundary covered by Laves phase particles and NiAl precipitates and  $L$  is the total length of the grain boundary:

$$\rho(\%) = \frac{l_1 + l_2 + l_3 + l_4 + \dots}{L} \times 100 \quad (1)$$

The value of  $\rho$  was calculated from the average of three BSE images of mechanically polished samples where the value of  $L$  was approximately 0.8  $\mu\text{m}$  in each sample.

Elevated temperature tensile tests were conducted at 760°C with an applied preload force of 50 N for specimens homogenized at 1250°C for 24 h and subsequently aged at 800°C for 0, 2.4, 24 or 240 h as described in Chapter 3. Specimens were polished on a turntable using successively finer silicon carbide abrasive paper up to 1200-grit, then with 0.3  $\mu\text{m}$  alumina powder dissolved in water. For all tests the initial strain rate was  $5 \times 10^{-4} \text{ s}^{-1}$ . Up to five tensile tests were performed for each heat treatment protocol. See Chapter 3 for details on testing methods and microstructural characterization. SEM images of the sample fracture surface were taken after tensile testing was complete.

Constant-stress creep tests were performed under a 35 MPa load at an elevated temperature of 760°C for specimens homogenized at 1250°C and then aged 0, 2.4, 24 or

240 h at 800°C. At least two tests were completed for each aging condition for a 500 h duration. To gain insights into strain rate behavior at longer time intervals, creep tests were conducted for aging conditions of 2.4 h, 24 h and 240 h and lasting for durations of 1000 h, 750 h and 800 h respectively.

To study the effect of temperature on creep rate, two constant-stress creep tests were performed under a 35 MPa load at elevated temperatures of 760°C and 700°C. Prior to creep testing, the specimens were homogenized at 1250°C and did not undergo heat treatment.

To explore the effects of straining at an elevated temperature on the microstructure of the alloy, microstructural analysis was performed on the specimens for each aging condition after the completion of a 500 h creep test using BSE images taken by the SEM as detailed in Chapter 3. Images were taken of three locations along each T-bone for each condition to compare precipitate quantity and size at a location where the sample was not strained (the head) and a location where the sample was strained (the gauge).

### 4.3 Results and Discussion

#### 4.3.1 Investigating presence of $\gamma'$ -Ni<sub>3</sub>Al (L1<sub>2</sub>) precipitates at 760°C

A bright-field TEM image of a precipitate located on the edge of a thin foil in a sample of Fe-20Cr-30Ni-2Nb-5Al (at. %) homogenized at 1250°C for 24 h, aged at 800°C for 24 h and crept for ~800 h at 760°C is shown in Figure 4.1 (a). A selected area diffraction pattern (SADP) taken from the f.c.c. matrix is shown in Figure 4.1 (b). The strong diffraction spots are from the L1<sub>2</sub> phase  $\gamma'$ -Ni<sub>3</sub>Al precipitate superlattice reflections, and the orientation relationship between the f.c.c. austenite matrix and the L1<sub>2</sub> phase is cube-on-cube, mimicking results of alloys with similar compositions to Fe-20Cr-30Ni-2Nb-5Al (at. %) that have exhibited L1<sub>2</sub>  $\gamma'$ -Ni<sub>3</sub>Al precipitates<sup>19,34,50</sup>. This result confirms that this precipitate is the  $\gamma'$ -Ni<sub>3</sub>Al L1<sub>2</sub> phase.

In prior studies the presence of  $\gamma'$ -Ni<sub>3</sub>Al was found after creep-rupture tests conducted at 750°C and under a 100 MPa load and were said to improve the alloy's creep properties<sup>20</sup>. However, the precipitate was not found at 800°C in an alloy of the same composition as the model alloy<sup>35</sup>. The current result confirming the presence of the  $\gamma'$ -Ni<sub>3</sub>Al precipitate at 760°C, supports the hypothesis that the model alloy has superior creep properties that are extended to an upper bound temperature of 760°C. Further work needs to be conducted to determine at what temperature Ni<sub>3</sub>Al particles are no longer stable.

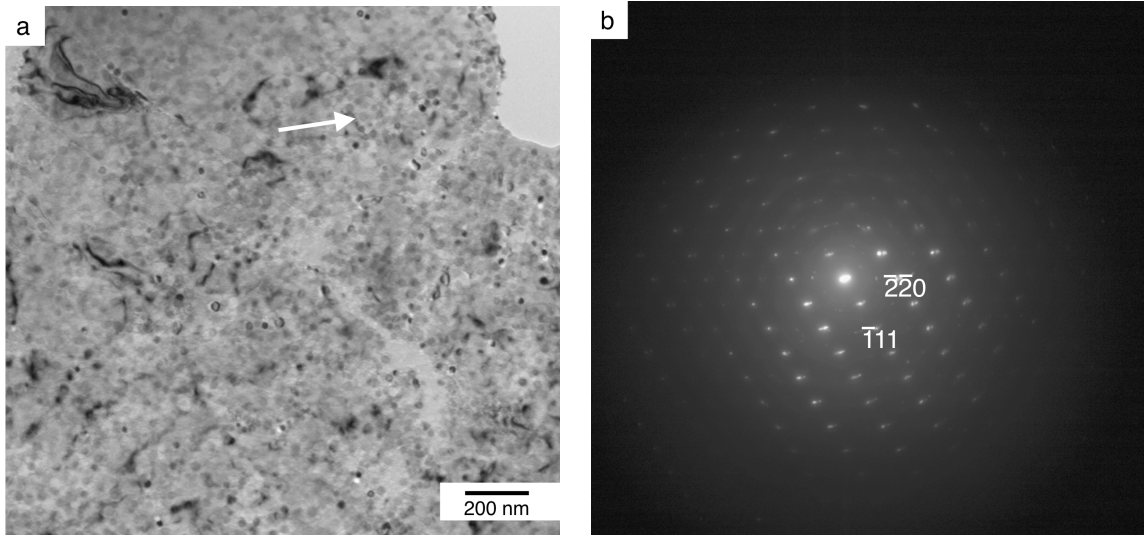


Figure 4.1: (a) Bright-field TEM image of Fe-20Cr-30Ni-2Nb-5Al (at. %) homogenized at 1250°C for 24 h, aged at 800°C for 24 h and crept for ~800 h at 760°C with an arrow indicating the matrix; (b) corresponding selected area diffraction pattern of the matrix showing  $\gamma'$ -Ni<sub>3</sub>Al (L1<sub>2</sub>) superlattice reflections.

#### 4.3.2 Characterizing the effects of aging time on alloy's microstructure

Figure 4.2 shows BSE images of the microstructure evolution of Fe<sub>2</sub>Nb Laves phase precipitates after a homogenizing anneal at 1250°C for 24 h and subsequent aging at 800°C for 2.4 h, 24 h, and 240 h. Fe<sub>2</sub>Nb Laves phase precipitates are common in AFAs<sup>10,13,16,18,19,51,52</sup>. It can be seen in Figure 4.2 (a) that after annealing at 1250°C, the alloy shows no precipitation in the single-phase f.c.c. matrix prior to aging. After aging for 2.4 h (b), 24 h (c), and 240 h (d), the alloy exhibits increasing quantities of fine dispersions of lightly contrasted Fe<sub>2</sub>Nb Laves phase precipitates in the SEM images. After aging for just 2.4 h, the Laves phase is present only on the grain boundaries, however after aging

for 24 h and 240 h at 800°C, in addition to appearing on the grain boundaries, the particles are also observed in the alloy's austenite matrix. The precipitates along the grain boundaries appear coarser than those in the interior of the grains in the matrix.

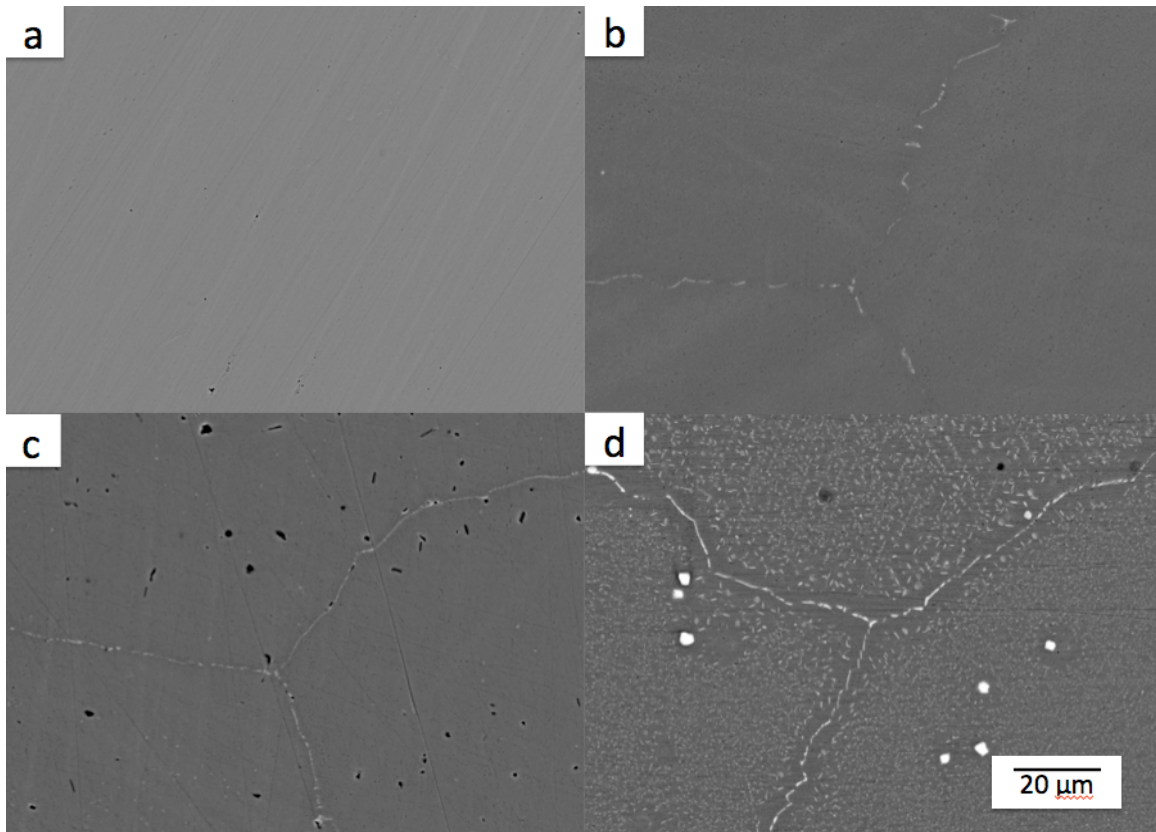


Figure 4.2: BSE SEM images of Fe-20Cr-30Ni-2Nb-5Al (at. %) homogenized at 1250°C for 24 h (a), then subsequently aged at 800°C for 2.4 h (b), 24 h (c), and 240 h (d). The light precipitates are the Laves phase.

Figure 4.2 (d) shows that after aging for 240 h, there is significant Laves phase precipitation in the matrix of the alloy and they have significantly increased in size compared to shorter duration heat treatments. A precipitate-free zone (PFZ) is visible

adjacent to the grain boundary in the sample aged for the longest duration. This supports prior studies' findings of the formation of a PFZ in aged Al alloys, which can arise either from a depletion of solute atoms proximal to the grain boundary, or from a depletion of lattice vacancies <sup>53</sup>. Images from a study on Fe-20Cr-30Ni-2Nb-5Al (at.%) that was creep tested at 750°C under a 100 MPa load, show a PFZ along the grain boundaries covered by alternating Fe<sub>2</sub>Nb and NiAl phase particles. They hypothesized that this effect was due to the formation of NiAl on the grain boundary, which caused a local Al depletion in the adjacent matrix, and that elimination of the PFZ may further improve the alloy's creep properties <sup>20</sup>.

Table 4.1 shows how the area fraction of grain boundary Fe<sub>2</sub>Nb Laves phase and NiAl precipitates changes with aging time. When the sample was fully solutionized at 1250°C but not heat treated, there is no grain boundary coverage and the alloy is single phase austenite. After a 2.4 h heat treatment at 800°C, the grain boundary area fraction increases to 42%. The grain boundary coverage is 69% for samples aged for 24 h and increases to 77% for samples aged 240 h. These grain boundary coverage values are consistent with prior work on the model alloy <sup>38</sup>.

*Table 4.1 Area fraction of grain boundary (GB) Laves phase and NiAl precipitates for Fe-20Cr-30Ni-2Nb-5Al (at. %) homogenized at 1250°C and aged at 800°C for 0, 2.4, 24 or 240 h. The GB area fraction is calculated from an average of three BSE images for each aging condition.*

<b>Aging time (h)</b>	<b>GB area fraction (%)</b>
0	0
2.4	42
24	69
240	77

#### *4.3.3 Effect of aging time on high temperature tensile behavior*

To study the effect of aging time on the model alloy's high temperature tensile behavior, tensile tests were conducted at different aging conditions at an elevated temperature and the results were compared to room temperature tensile tests.

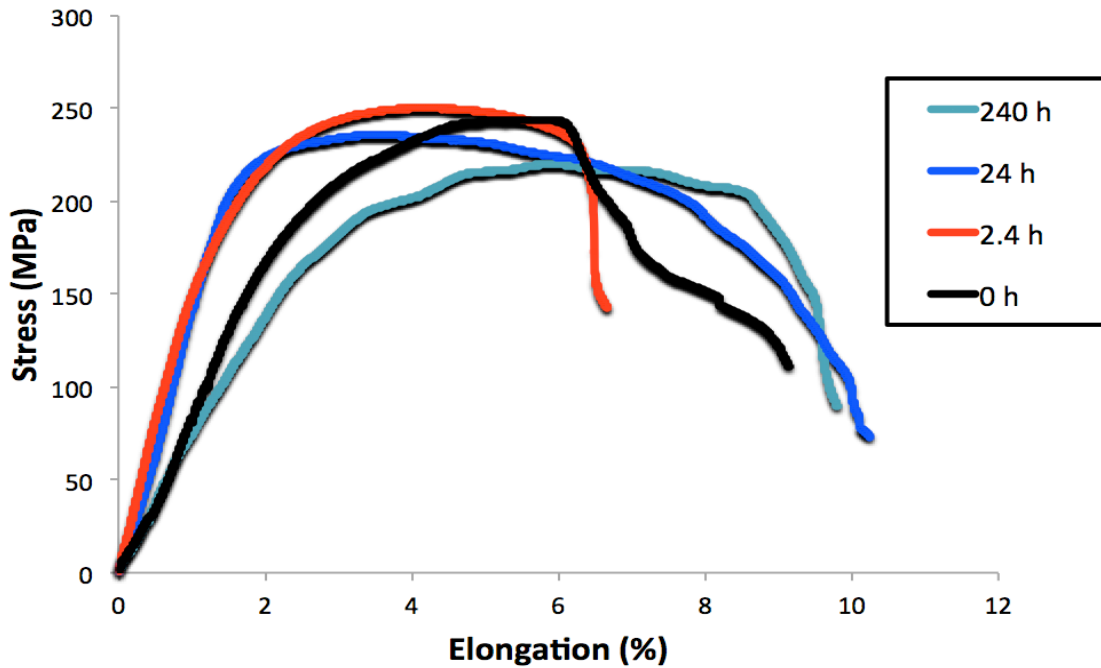


Figure 4.3: High temperature tensile curves of Fe-20Cr-30Ni-2Nb-5Al (at. %) homogenized at 1250°C for 24 h and subsequently aged at 800°C for 0, 2.4, 24 or 240 h as indicated. Tensile tests were conducted at 760°C with an initial strain rate of  $5 \times 10^{-4} \text{ s}^{-1}$ . Results are the average of at least three tests at each condition.

Figure 4.3 shows high temperature tensile curves of Fe-20Cr-30Ni-2Nb-5Al (at. %) conducted at 760°C with an initial strain rate of  $5 \times 10^{-4} \text{ s}^{-1}$ . Prior to tensile testing samples were homogenized at 1250°C for 24 h and subsequently aged at 800°C for 0, 2.4, 24 or 240 h. At least three tests were conducted at each condition and the results averaged. Table 4.2 provides a summary of the average high temperature yield strength (YS), high temperature ultimate tensile strength (UTS), and elongation to failure ( $\epsilon_f$ ) for the samples.

*Table 4.2 High temperature yield strength (YS), high temperature ultimate tensile strength (UTS), and elongation to failure ( $\epsilon_f$ ) for Fe-20Cr-30Ni-2Nb-5Al (at. %) homogenized at 1250°C for 24 h, heat treated at 800°C and strained under tension at 760°C with an initial strain rate of  $5 \times 10^{-4} \text{ s}^{-1}$ . Results are the average of at least three tests at each condition.*

<b>Aging time (h)</b>	<b>YS (MPa)</b>	<b>UTS (MPa)</b>	<b><math>\epsilon_f</math> (%)</b>
0	188	249	7.7
2.4	225	252	5.7
24	202	237	8.9
240	166	224	9.6

Overall, the high temperature YS, UTS and elongations to failure were significantly lower when compared to results of tensile tests conducted at room temperature on the model alloy in prior studies and no work-hardening was observed<sup>38</sup>. For the 2.4 h aged sample no discontinuation was observed as compared to the 2.4 h room temperature tensile sample which exhibited an upper and lower yield point and a 5% Lüder's strain. Interestingly, the room temperature YS for the 2.4 h sample has the lowest value of all the heat treated samples (2.4 h, 24 h, 240 h), but has the highest value of all samples tested, including the homogenized sample, for the high temperature tests. This may be attributed to the presence of fine Laves phase precipitates pinning

dislocations and strengthening the alloy. As the precipitates increase in size and coarsen, the strengthening properties decrease.

The sample aged for 240 h exhibited the lowest yield strength (166 MPa) of all the heat treatments tested, even when compared to the homogenized sample which was not heat treated and had a yield strength of 188 MPa. This poor tensile performance can possibly be attributed to the 240 h anneal having the highest area fraction of grain boundary  $\text{Fe}_2\text{Nb}$  Laves phase and NiAl precipitates of all samples tested, with 77% of the grain boundary covered, and a significant PFZ visible adjacent to the grain boundaries as seen in Figure 4.2 (d). In previous studies studying creep-rupture curves and the resulting microstructure of creep-rupture tests conducted at 750°C and 100 MPa on an alloy with the same composition as the model alloy, a PFZ was also found adjacent to the grain boundaries. The authors posited that deformation occurred primarily along the PFZ rather than uniformly throughout the grains and that elimination of the PFZ may further improve the creep properties of the alloy <sup>20</sup>. This explanation is further supported by Figure 4.4 of the fracture surface for Fe-20Cr-30Ni-2Nb-5Al (at. %) after being homogenized at 1250°C for 24 h, aged at 800°C for 240 h and tensile tested at 760°C, and shows fracture occurring along the grain boundary of the alloy and not the matrix. The fracture surface shows a visible layer of oxide due to the high temperature the alloy was exposed to during tensile testing.

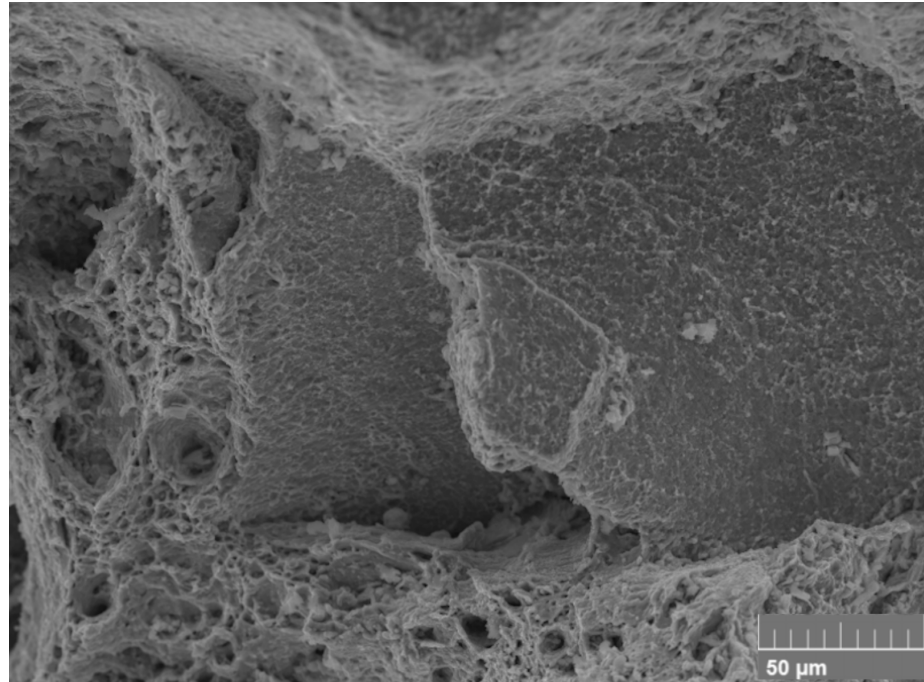


*Figure 4.4: BSE image of fracture surface for Fe-20Cr-30Ni-2Nb-5Al (at. %) after being homogenized at 1250°C for 24 h, aged at 800°C for 240 h and strained under tension at 760°C with an initial strain rate of  $5 \times 10^{-4} \text{ s}^{-1}$ .*

#### 4.3.4 Effect of aging time on post-creep test microstructure

Figure 4.5 shows BSE images of the microstructure evolution of  $\text{Fe}_2\text{Nb}$  Laves phase and  $\text{NiAl}$  precipitates after a homogenizing anneal at 1250°C for 24 h, subsequent aging at 800°C for 2.4 h, 24 h, and 240 h and crept at 760°C for 500 h under a load of 35 MPa. The light contrast particles are the Laves phase and the dark contrast particles are  $\text{NiAl}$  precipitates. It can be seen in Figure 4.2 (a) that after the homogenization anneal there is no evident precipitation, and after the completion of the 500 h creep test at 760°C, the alloy exhibits fine dispersions of lightly contrasted  $\text{Fe}_2\text{Nb}$  Laves phase and

darkly contrasted NiAl precipitates in the austenite matrix and on the grain boundaries of the alloy. These two precipitates are commonly found in heat treated and strained AFAs

10,42,43

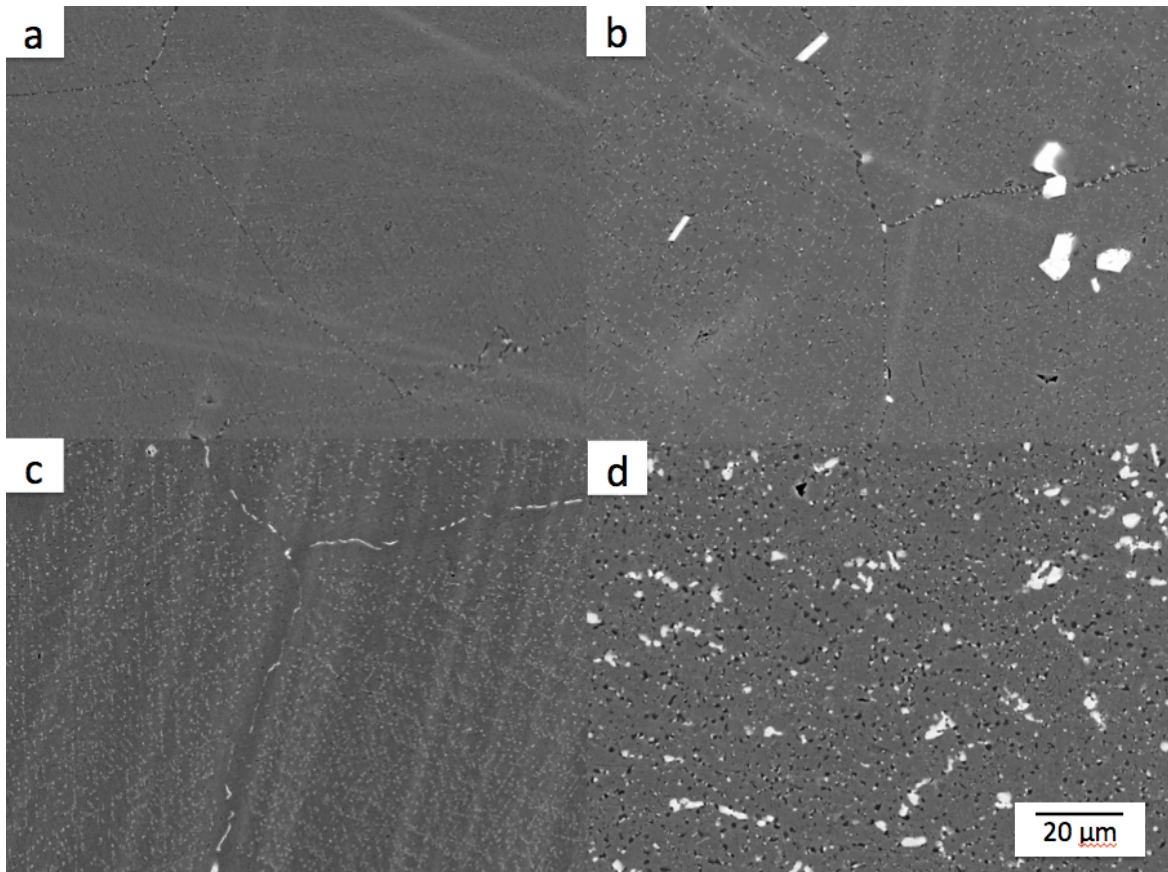


Figure 4.5: BSE SEM images of Fe-20Cr-30Ni-2Nb-5Al (at. %) homogenized at 1250°C for 24 h (a), then subsequently aged at 800°C for 2.4 h (b), 24 h (c), 240 h (d) and crept at 760°C for 500 h under a load of 35 MPa in air. The light precipitates are the Laves phase and the dark precipitates are NiAl precipitates.

As the aging time of the samples increases from 2.4 h (b) to 24 h (c) and then 240 h (d), the alloy exhibits increasing size and quantities of both the Fe<sub>2</sub>Nb Laves phase and

NiAl precipitates on the grain boundaries and in the matrix. The precipitates along the grain boundaries appear coarser than those in the interior of the grains in the matrix. A PFZ is visible adjacent to the grain boundary in the sample aged for 2.4 h, which becomes even more clearly visible in the sample aged for 24 h prior to creep. Figure 4.5 (d) shows that for the sample aged for 240 h and subsequently creep tested, there is significant Laves phase and NiAl precipitation in the matrix of the alloy and the precipitates have significantly increased in size compared to shorter duration heat treatments.

Comparing the images of samples heat treated for the same duration and taken prior to creep in Figure 4.2 to those imaged after creep testing was completed in Figure 4.5, it is evident that precipitation occurred during the 500 h long creep test. A side-by-side comparison of a solutionized sample and samples aged for 240 h prior to creep and after creep testing can be seen in Figure 4.6 as an example of the precipitate evolution that occurred in each sample tested. The number and size of precipitated particles increased over the duration of the creep tests both in the matrix and on the grain boundaries of all specimens tested. In the samples imaged prior to creep testing NiAl precipitates were either completely absent or few in number compared to the Fe<sub>2</sub>Nb Laves phase. This is in contrast to the images taken after creep testing, where NiAl precipitates were present in every specimen, including even the sample that was fully solutionized prior to creep and exhibited no visible signs of precipitation. These results are not surprising given the fact that the creep testing temperature of 760°C was only

40°C lower than that of the heat treatment temperature of 800°C, so continued precipitation during the creep test was expected.

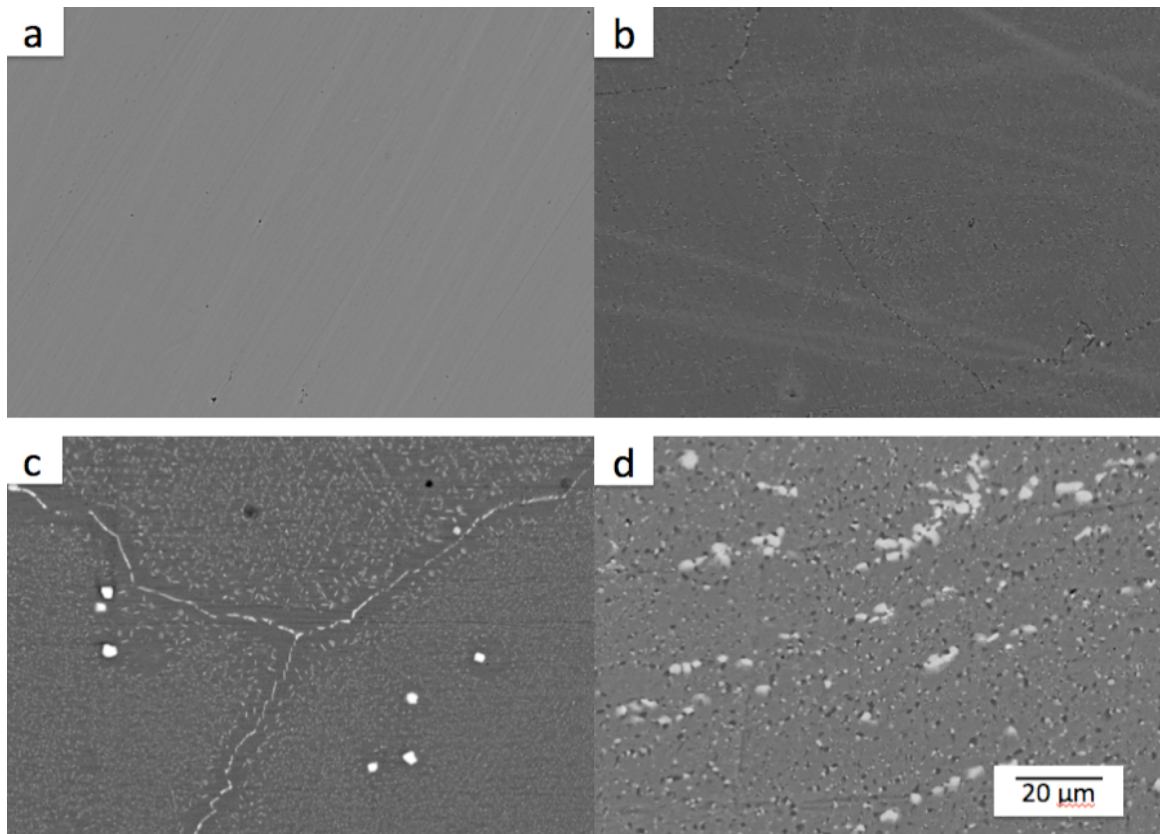
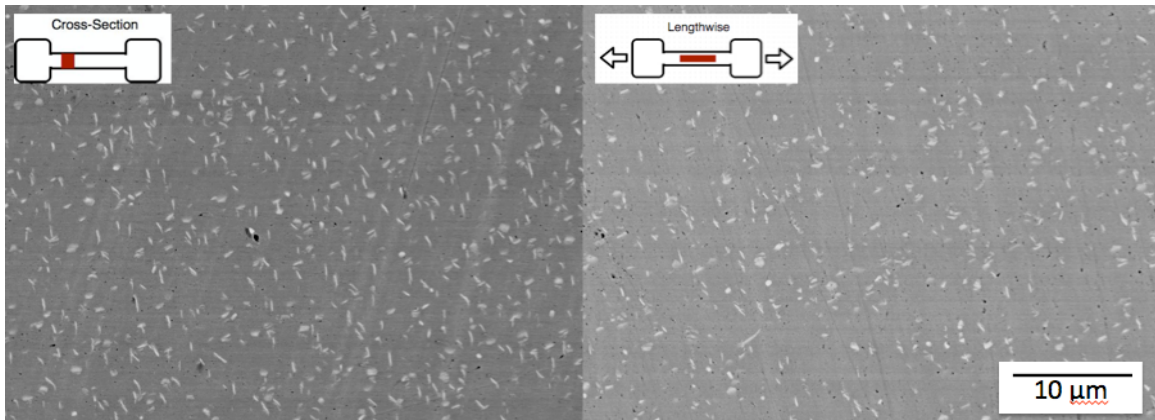


Figure 4.6: BSE SEM images of Fe-20Cr-30Ni-2Nb-5Al (at. %) homogenized at 1250°C for 24 h prior to creep (a) and after creep testing (b); homogenized at 1250°C for 24 h and aged at 800°C for 240 h prior to creep (c) and after creep testing (d). Constant-stress creep tests were conducted at 760°C for 500 h under a load of 35 MPa in air. The light precipitates are the Laves phase and the dark precipitates are NiAl precipitates.

BSE SEM images were taken at three locations along each T-bone for each post-creep microstructural analysis specimen in order to compare precipitation properties at a

location where the sample was not strained (the head) and a location where the sample was strained (the gauge) as well as lengthwise along the gauge to determine if there were directional precipitation differences. Figure 4.7 shows that the precipitate structure in the cross-section of the gauge evolved in a similar way to the structure lengthwise along the gauge in images taken from the same crept T-bone sample.



*Figure 4.7: BSE SEM images of Fe-20Cr-30Ni-2Nb-5Al (at. %) homogenized at 1250°C for 24 h and subsequently aged at 800°C for 2.4 h and crept at 760°C for 500 h under a load of 35 MPa in air. Both images were taken from the gauge of the specimen with the left taken as a cross-section and the right lengthwise as indicated.*

Figure 4.8 shows an image taken from the gauge of a specimen (left), where the sample saw both the temperature and stress, and an image taken from the same T-bone sample's head (right) that saw only the temperature but not the strain. The precipitate structure of the gauge sample that had seen the stress of the creep test was significantly different from the smaller and less coarse precipitates found in the head of the T-bone sample that had only seen the same temperature but not the stress throughout the duration

of the creep test. Overall, the precipitate structure evolved in a similar way in cross-sectional and lengthwise samples taken from the gauge, but were less evolved in samples taken from the head of the T-bone.

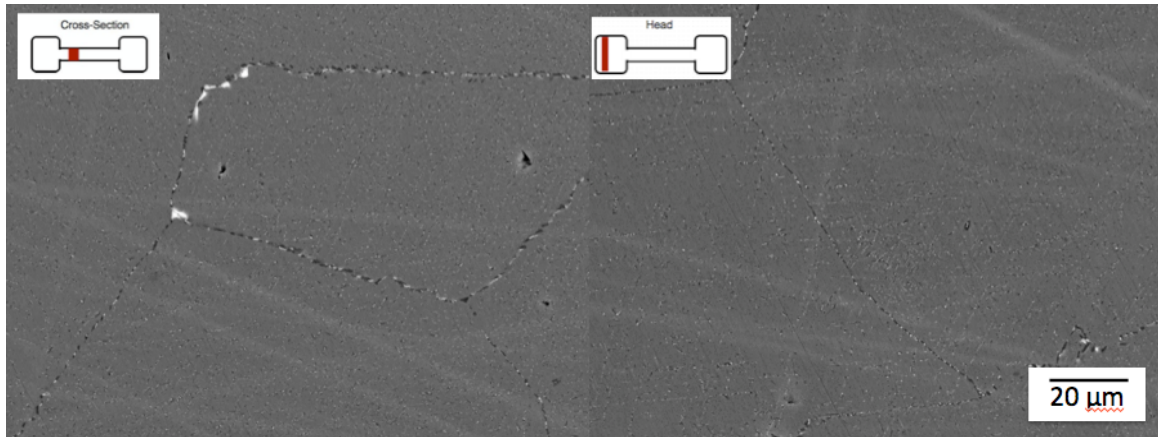


*Figure 4.8: BSE SEM images of Fe-20Cr-30Ni-2Nb-5Al (at. %) homogenized at 1250°C for 24 h and creeped at 760°C for 500 h under a load of 35 MPa in air. The left image was taken from the gauge of the specimen with the left taken from the head as indicated.*

#### *4.3.5 Effect of aging time on constant-stress creep properties*

The initial 5 h and full 500 h duration of constant-stress creep curves conducted at 760°C and 35 MPa in air for Fe-20Cr-30Ni-2Nb-5Al (at. %) are shown in Figure 4.9 and Figure 4.10 respectively. Prior to creep testing, each specimen was homogenized at 1250°C for 24 h and subsequently aged at 800°C for 0, 2.4, 24 or 240 h. Two creep tests were performed for each aging protocol, and the creep curves for all replicates can be found in Appendix III. These creep test conditions were chosen for this investigation to fall within the U.S. Department of Energy's goal of developing materials technology

needed for the construction of the critical components of coal-fired boilers and turbines that are capable of operating with steam at temperatures of 760°C and pressures of 35 MPa<sup>7-9</sup>.

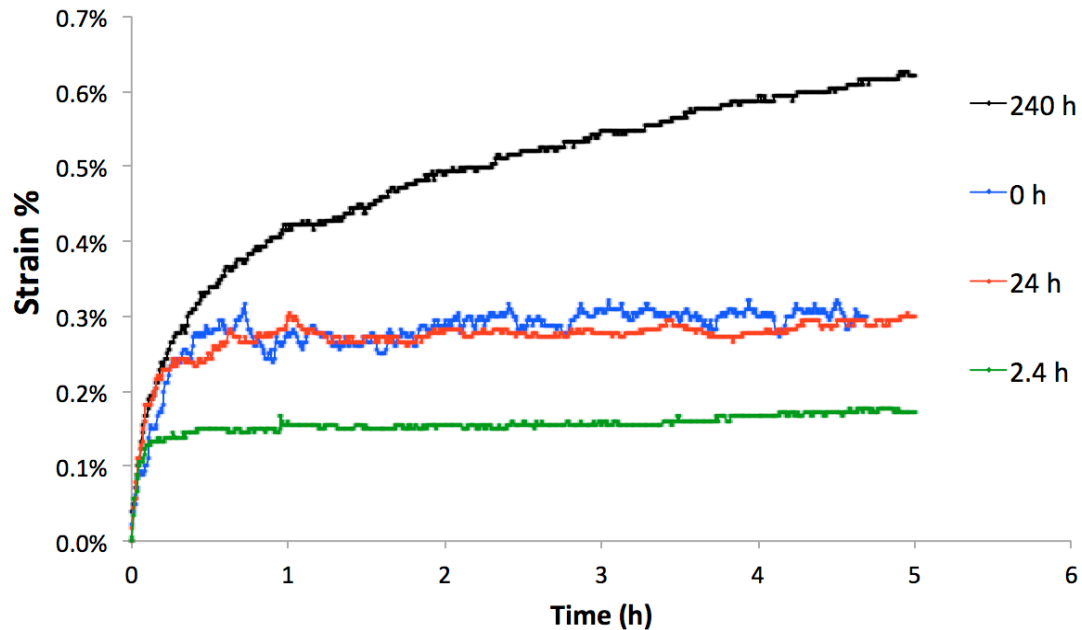
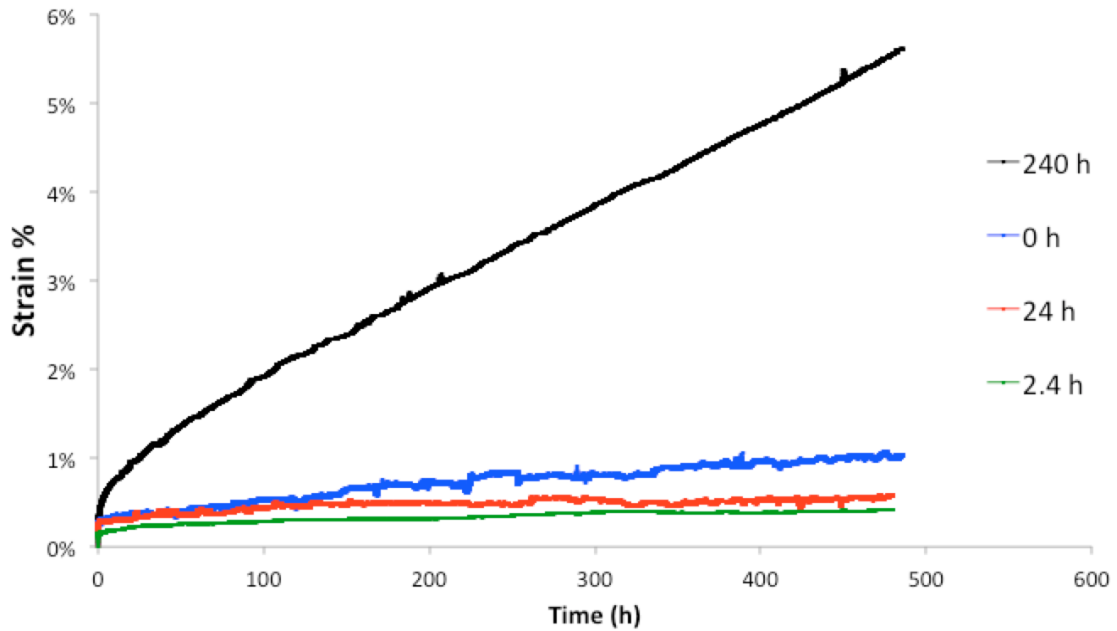


Figure 4.9: Initial five hours of constant-stress creep curves for Fe-20Cr-30Ni-2Nb-5Al (at. %) conducted at 760°C under a 35 MPa load in air. Specimens were homogenized at 1250°C for 24 h and subsequently aged at 800°C for 0, 2.4, 24 or 240 h prior to creep testing. Two creep tests were performed for each aging protocol.



*Figure 4.10: Constant-stress creep curves for Fe-20Cr-30Ni-2Nb-5Al (at. %) conducted at 760°C for 500 h under a 35 MPa load in air. Specimens were homogenized at 1250°C for 24 h and subsequently aged at 800°C for 0, 2.4, 24 or 240 h prior to creep testing. Two creep tests were performed for each aging protocol.*

During the initial creep phase, the samples heat treated for 0 h and 24 h had similar primary creep rates, which were higher than the primary creep rate of the 2.4 h aged samples. However, they diverged in their secondary creep rate with the homogenized samples exhibiting a significantly higher secondary creep rate and reaching 1.1% strain at the completion of the test, while the samples aged for 24 h only reached 0.6% strain. This result is contrary to that found in prior creep studies on this alloy, which found lower creep rates for the homogenized material when compared to aged

specimens<sup>20</sup> as well as suggestions that the NiAl and Laves phase don't show strong precipitation hardening at high temperatures and therefore don't contribute to creep strength<sup>54,55</sup>.

The samples aged for 2.4 h exhibited a similar secondary creep rate to the 24 h aged samples, and the lower overall strain of 0.4% compared to the 24 h samples' 0.6% can be attributed to the lower primary creep rate. This was an unusual finding because the area fraction of grain boundary Laves phase and NiAl precipitates was significantly higher, 69% compared to 42 % for the 24 h and 2.4 h aged samples, respectively and the size of the precipitates was also significantly larger. The samples aged for 240 h exhibited the highest primary and secondary creep rates with an overall strain reaching 5.6% after 500 h of undergoing creep testing. This result was unsurprising given the 77% grain boundary coverage and large size of coarsened Laves phase and NiAl precipitates evident in both the matrix and along the specimen's grain boundaries.

Overall, the creep rates correlate well with the measured high temperature yield strengths of the alloy as summarized in Table 4.2, with faster creep rates correlating with lower yield strengths. This result is surprising because prior work has found that creep rate does not correlate well with yield strength<sup>18,21,54</sup>.

To begin investigating the alloy's long-term creep properties, three constant-stress creep tests were conducted at 760°C and 35 MPa in air for Fe-20Cr-30Ni-2Nb-5Al (at. %) for durations above 500 h, and the resulting creep curves are shown in Figure 4.11.

Prior to creep testing, each specimen was homogenized at 1250°C for 24 h and subsequently aged at 800°C for 2.4, 24 or 240 h.

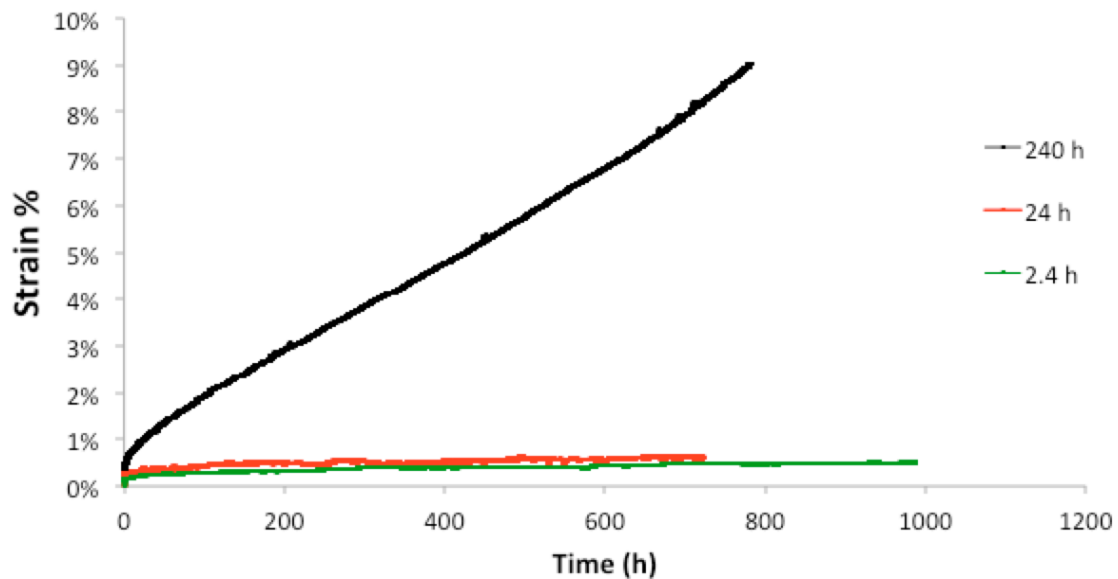


*Figure 4.11: Long-term constant-stress creep curves for Fe-20Cr-30Ni-2Nb-5Al (at. %) conducted at 760°C under a 35 MPa load in air for durations lasting longer than 500 h. Specimens were homogenized at 1250°C for 24 h and subsequently aged at 800°C for 2.4, 24 or 240 h prior to creep testing.*

The highest strain was reached by the sample aged for 240 h, with an overall strain of 9.1%. The trend of the 2.4 h and 24 h samples exhibiting a similar secondary creep rate, as seen for the first 500 h of the creep test, continued at longer time intervals of 720 h and 1000 h with the 24 h sample reaching 0.6% strain and the 2.4 h aged sample reaching a 0.5% strain, respectively. Further work on long-term creep tests and post-

creep test microstructural analysis will be necessary to explore secondary creep properties and duration to creep-rupture.

#### 4.3.6 *Effect of aging temperature on constant-stress creep rate*

To investigate how the alloy's creep rates changed with temperature, two constant-stress creep tests were conducted at 760°C and 700°C under a 35 MPa load and the resulting creep curves are shown in Figure 4.12. Prior to creep testing specimens were homogenized at 1250°C for 24 h but not heat treated.

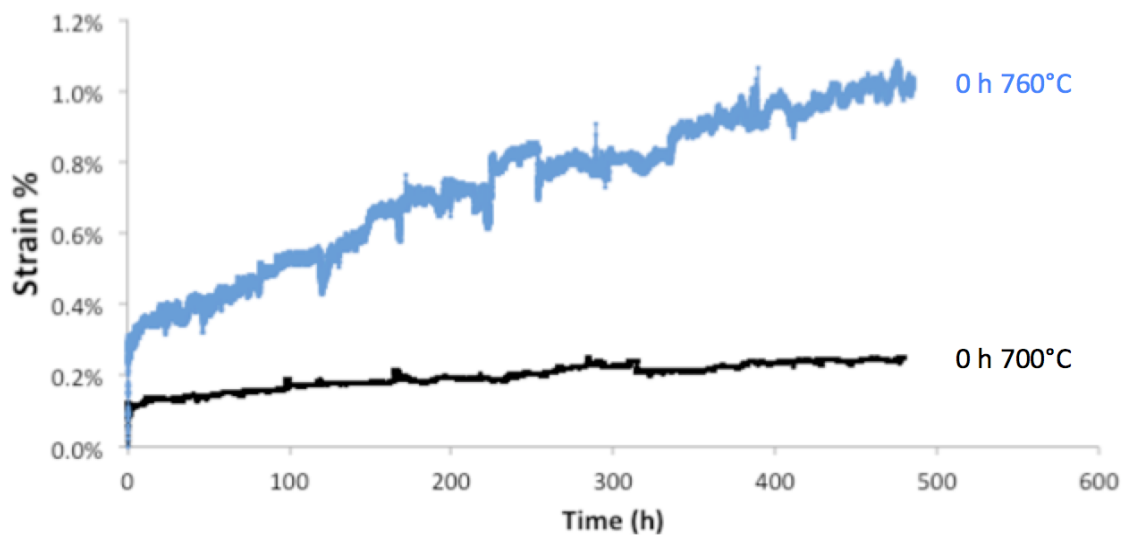


Figure 4.12: Constant-stress creep curves for Fe-20Cr-30Ni-2Nb-5Al (at. %) conducted at 760°C and 700°C under a 35 MPa load. Specimens were homogenized at 1250°C for 24 h but not heat treated prior to creep testing.

The specimen creep tested at 700°C exhibited a significantly lower strain compared to the specimen tested at 760°C, with strains of 0.2% and 1.1%, respectively. This is an expected result as creep rates are temperature dependent, with high creep rates correlating with higher test temperatures <sup>21,54,56</sup>. Creep rate investigations at temperatures above 760°C remain to be investigated in future work.

## CHAPTER 5 CONCLUSIONS

After annealing at 1250°C, Fe-20Cr-30Ni-2Nb-5Al (at. %) showed no precipitation in the single-phase f.c.c. matrix prior to aging. After aging for 2.4 h, 24 h, and 240 h, the alloy exhibited increasing quantities of fine dispersions of lightly contrasted  $\text{Fe}_2\text{Nb}$  Laves phase precipitates. After aging for just 2.4 h, the Laves phase was present only on the grain boundaries, however after aging for 24 h and 240 h at 800°C, in addition to appearing on the grain boundaries, the particles were also observed in the alloy's austenite matrix. The precipitates along the grain boundaries appeared coarser than those in the interior of the grains in the matrix. A precipitate-free zone (PFZ) was visible adjacent to the grain boundary in the sample aged for 240 h.

The  $\text{L1}_2$  phase  $\gamma'$ - $\text{Ni}_3\text{Al}$  precipitate was found at 760°C in a sample of Fe-20Cr-30Ni-2Nb-5Al (at. %) homogenized at 1250°C for 24 h, aged at 800°C for 24 h and crept for  $\sim$ 800 h at 760°C. Prior to this finding  $\gamma'$ - $\text{Ni}_3\text{Al}$  had only been found at 750°C and was not found at 800°C in an alloy of the same composition.

The area fraction of grain boundary  $\text{Fe}_2\text{Nb}$  Laves phase and  $\text{NiAl}$  precipitates increased with aging time. When the sample was fully solutionized at 1250°C, there was no grain boundary coverage. After aging for 2.4 h at 800°C, the grain boundary area fraction increased to 42%. The grain boundary coverage was 69% for samples aged for 24 h and increased to 77% for samples aged 240 h.

The high temperature YS, UTS and elongations to failure of tensile tests conducted at 760°C were significantly lower when compared to results of tensile tests

conducted at room temperature. The room temperature YS for the 2.4 h sample had the lowest value of all the heat treated samples (2.4 h, 24 h, 240 h), but had the highest value of all samples tested for the tests conducted at 760°C. The sample aged for 240 h exhibited the lowest yield strength of all the heat treatments tested.

The number and size of precipitated  $\text{Fe}_2\text{Nb}$  Laves phase and NiAl precipitate particles increased over the course of the 500 h constant-stress creep tests both in the matrix and on the grain boundaries of all specimens tested.

The precipitate structure evolved in a similar way in cross-sectional and lengthwise samples taken from the gauge of each crept sample, but the structure was less evolved in samples taken from the head of the T-bone that had only been exposed to the temperature but not the stress of the creep test.

Specimens heat treated for 0 h and 24 h had similar primary creep rates, which were higher than the primary creep rate of the 2.4 h aged samples. However, they diverged in their secondary creep rate, with the homogenized samples exhibiting a significantly higher secondary creep rate and reaching 1.1% strain at the completion of the test, while the samples aged for 24 h only reached 0.6% strain. Samples aged for 2.4 h exhibited a similar secondary creep rate to the 24 h aged samples. Samples aged for 240 h exhibited the highest primary and secondary creep rates with an overall strain of 5.6%.

High temperature creep rates correlated well with high temperature yield strengths of the alloy, with faster creep rates correlating with lower yield strengths.

The 700°C creep test exhibited a significantly lower creep rate compared to the 760°C creep test, with strains of 0.2% and 1.1%, respectively.

## CHAPTER 6 FUTURE WORK

Future work should be divided amongst several focus areas:

1. Although three longer-term constant-stress creep tests were conducted for durations above 500 h, further investigations into the Fe-20Cr-30Ni-2Nb-5Al (at. %) alloy's short and long-term duration creep rates and post-creep microstructural analysis is necessary to explore secondary creep properties and time to creep-rupture.
2.  $\text{Ni}_3\text{Al}$   $\text{L}1_2$  particles were found in TEM images taken of samples crept at 700-760°C, but the upper temperature bound at which  $\text{Ni}_3\text{Al}$  remains stable and provides superior creep properties is yet to be determined. Additionally, in order to characterize how Fe-20Cr-30Ni-2Nb-5Al (at. %) performs at a range of high temperatures above 760°C and identify the effect of temperature on creep rates, further constant-stress creep tests at temperatures above 760°C should be performed and the presence of  $\text{Ni}_3\text{Al}$  investigated by imaging with TEM.
3. The effect of adding a small amount of silicon to Fe-20Cr-30Ni-2Nb-5Al (at. %) should be studied. More particularly, since the addition of silicon has been shown to increase the formation of Laves phase in several steels, the creep properties of the model alloy with 0.2% added silicon should be studied. The same aging protocol used for the non-silicon doped material should be administered and creep tests conducted at 760°C

and 35 MPa in order to compare the obtained creep rates and characterized microstructure to those obtained in this investigation.

## APPENDICES

### Appendix I: Constant Stress Derivation

$$x = \frac{a}{1+b\theta} \left[ \cos(\theta) + \frac{b \sin(\theta)}{1+b\theta} \right] \quad (1)$$

$$y = \frac{a}{1+b\theta} \left[ \sin(\theta) - \frac{b \cos(\theta)}{1+b\theta} \right] \quad (2)$$

$$a = \frac{r_0 L_0}{L_0 - R\theta_0} \quad \text{and} \quad b = \frac{R}{L_0 - R\theta_0}$$

To maintain a constant stress, the following condition must be satisfied:

$$rL = \text{constant} = r_0 L_0 \quad (1)$$

Where:

$L_0$  = initial specimen length

$r_0$  = initial value of  $r$  (instantaneous moment arm of the applied weight)

The instantaneous specimen length can be written as:

$$L = L_0 + (\theta - \theta_0)R \quad (2)$$

Where:

$\theta_0$  = angle for initial positioning of constant-stress cam

Eliminating  $L$  from equations (1) and (2) gives you the equation for the profile of a constant-stress cam:

$$r = \frac{r_0 L_0}{L_0 + R(\theta - \theta_0)} \quad (3)$$

This equation needs to be transformed into fixed a Cartesian coordinate system for ease of use in terms of  $x$  and  $y$ .

$$x = r \cos(\theta) + z \sin(\theta) \quad (4)$$

$$y = r \sin(\theta) - z \cos(\theta) \quad (5)$$

$$\frac{dx}{dy} = -\tan(\theta) \quad (6)$$

Eliminating  $x$  and  $y$  from the equations:

$$z = -dr/d\theta = \frac{r_0 L_0 R}{[L_0 + R(\theta - \theta_0)]^2} \quad (7)$$

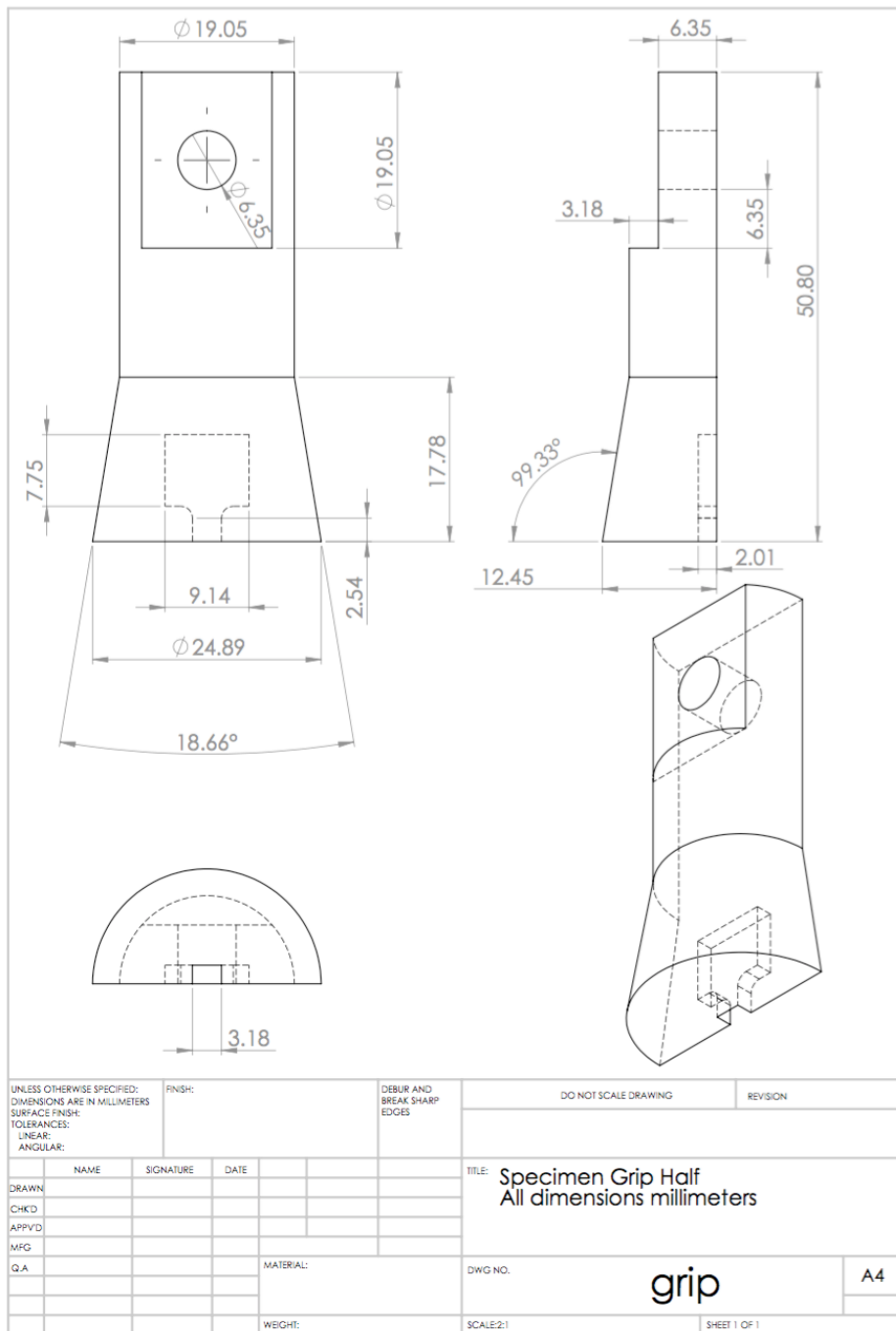
Substituting the above equation and equation (3) into equations (4) and (5) yields the fixed coordinates of the constant-stress cam in terms of the single parameter  $\theta$ :

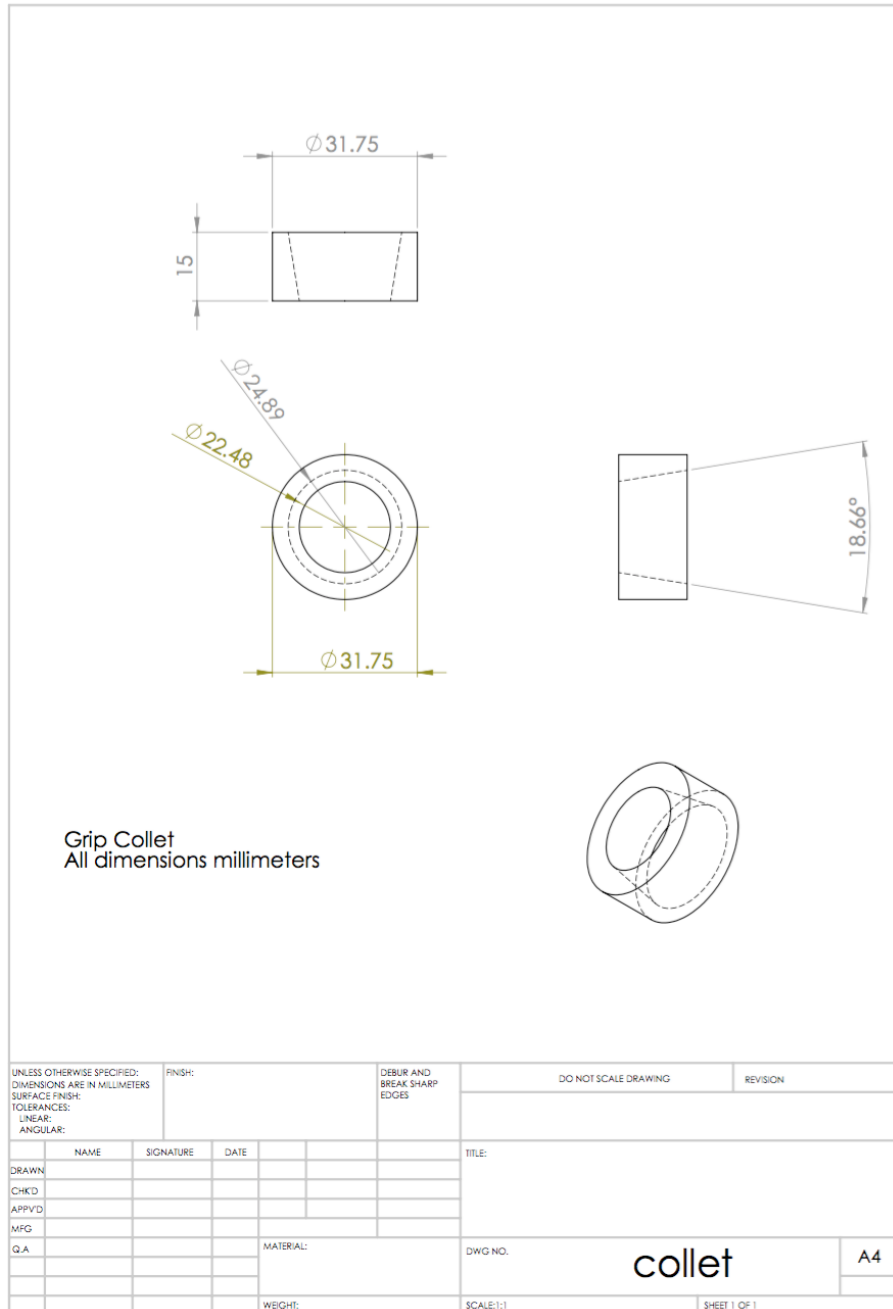
$$x = \frac{a}{1 + b\theta} \left[ \cos(\theta) + \frac{b \sin(\theta)}{1 + b\theta} \right] \quad (8)$$

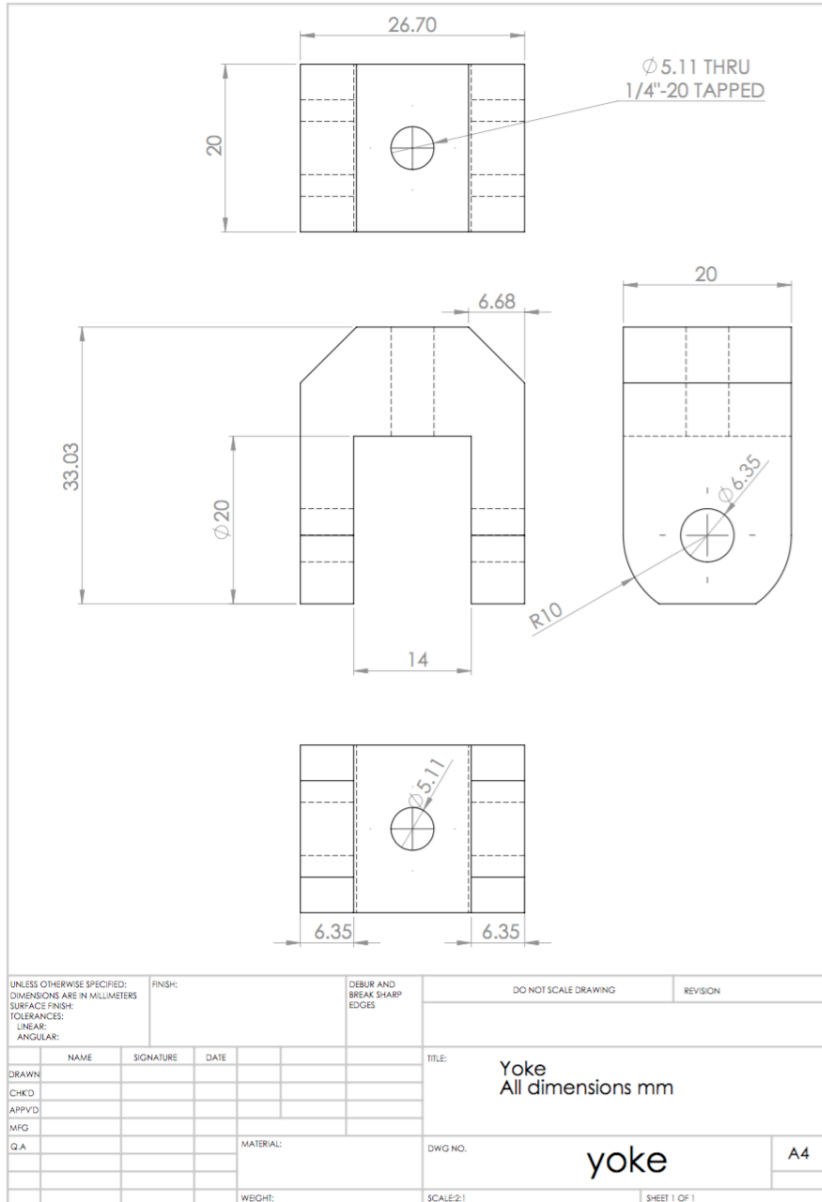
$$y = \frac{a}{1 + b\theta} \left[ \sin(\theta) - \frac{b \cos(\theta)}{1 + b\theta} \right] \quad (9)$$

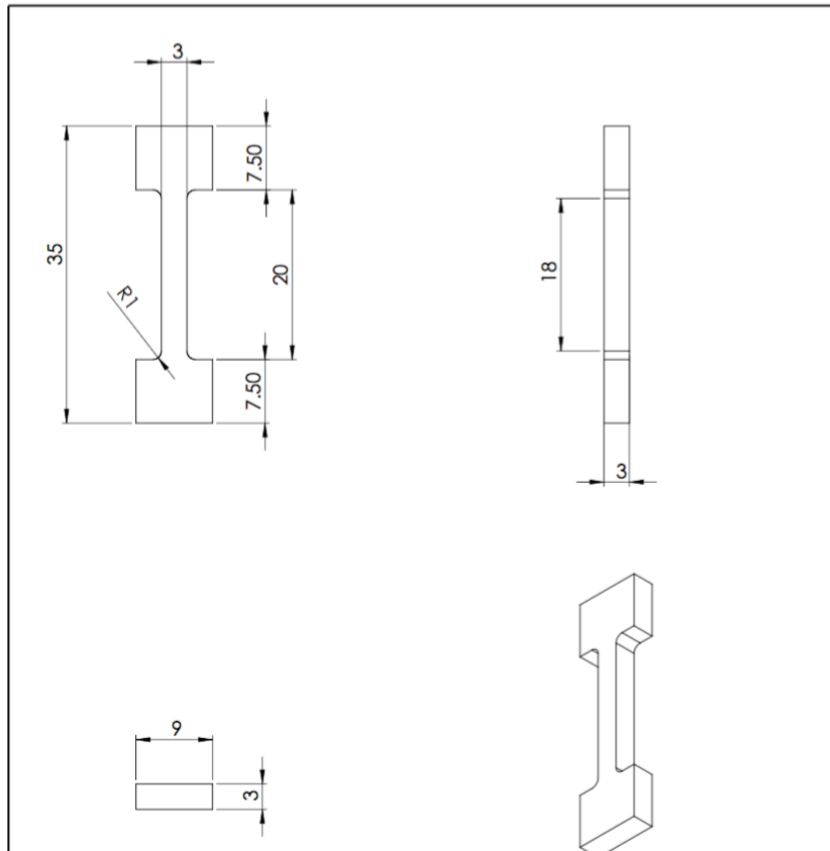
$$\text{Where: } a = \frac{r_0 L_0}{L_0 - R\theta_0} \text{ and } b = \frac{R}{L_0 - R\theta_0}$$

## Appendix II: Custom CAD files for Creep Rig



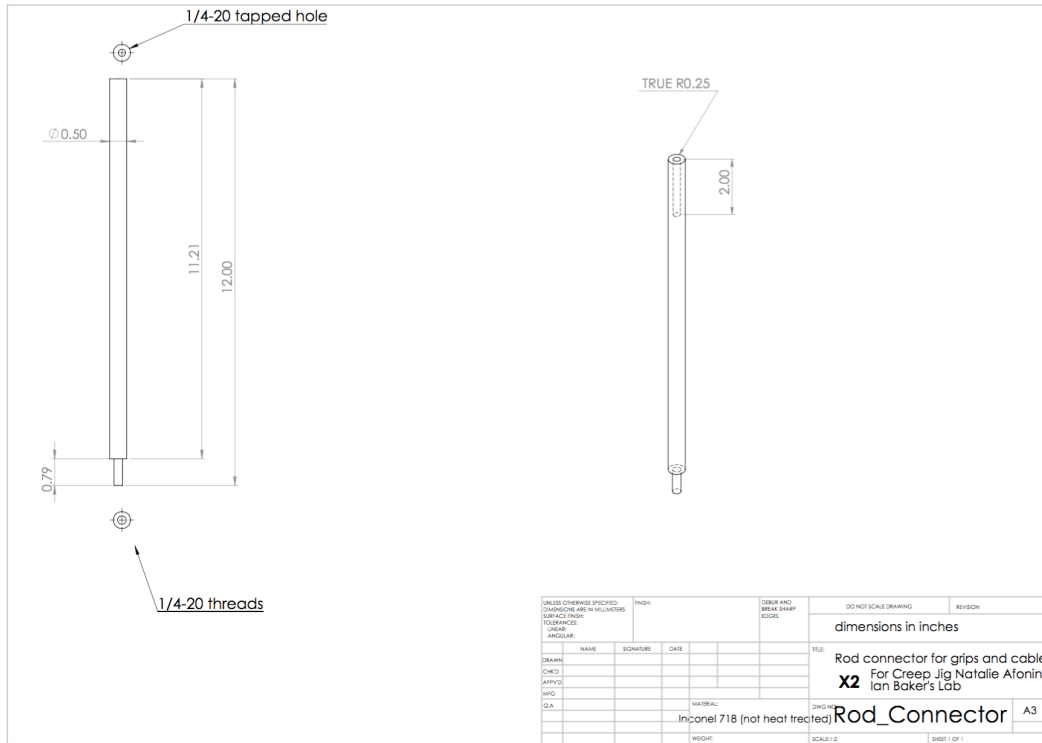


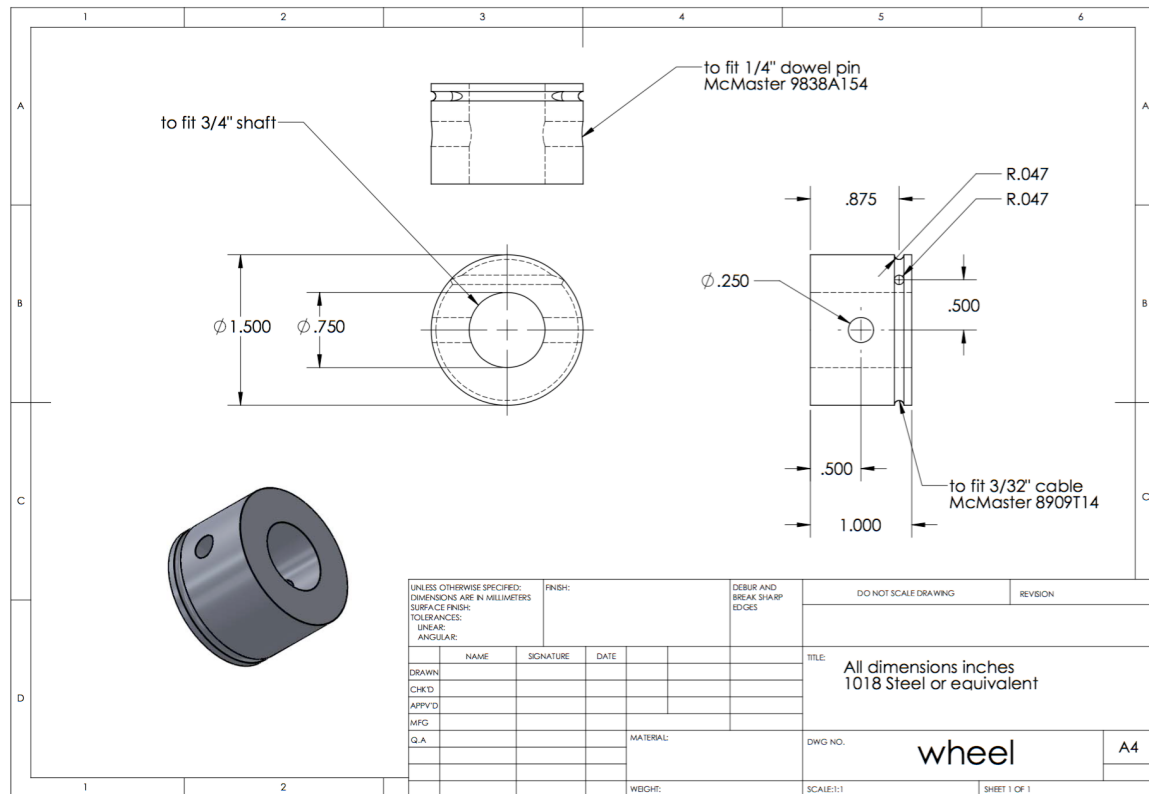


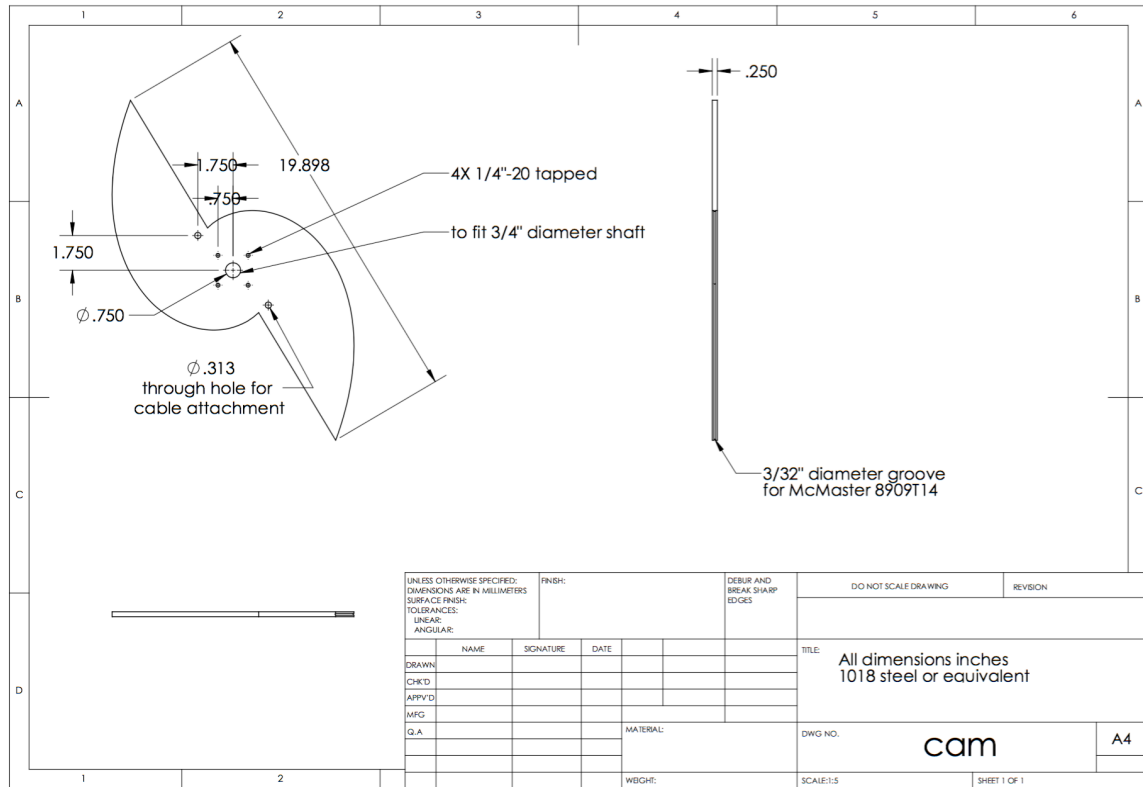


Tensile Specimen  
All dimensions millimeters

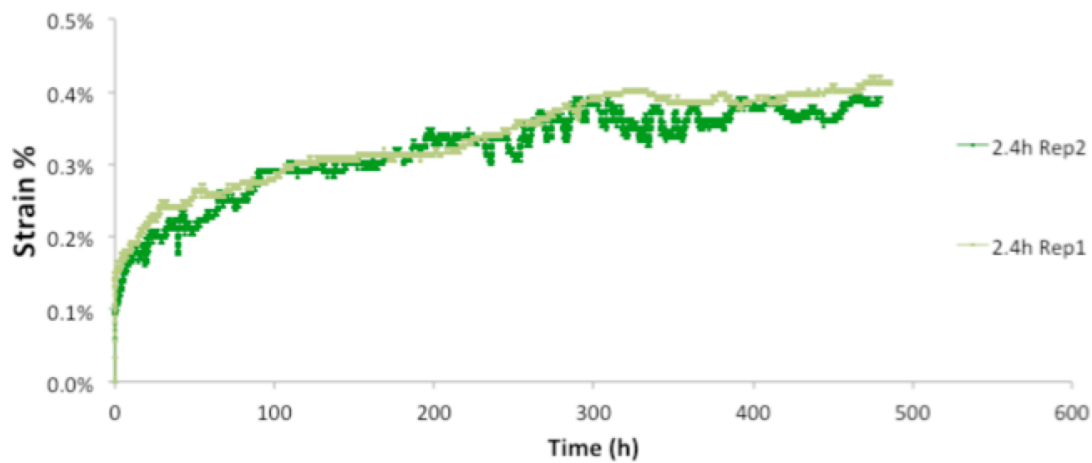
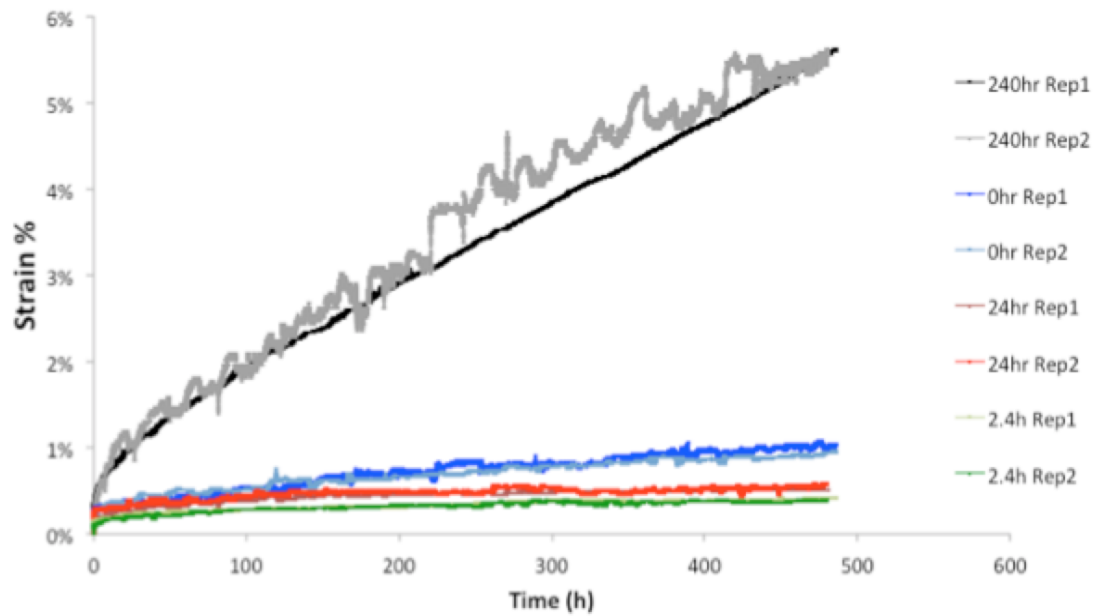
UNLESS OTHERWISE SPECIFIED: DIMENSIONS ARE IN MILLIMETERS SURFACE FINISH: TOLERANCES: LINEAR: ANGULAR:			FINISH:		DEBUR AND BREAK SHARP EDGES	DO NOT SCALE DRAWING		REVISION
NAME	SIGNATURE	DATE	MATERIAL:	WEIGHT:		TITLE:		
DRAWN								
CHKD								
APV'D								
MFG								
Q.A.					DWG NO.	specimen		A4
					SCALE:1	SHEET 1 OF 1		

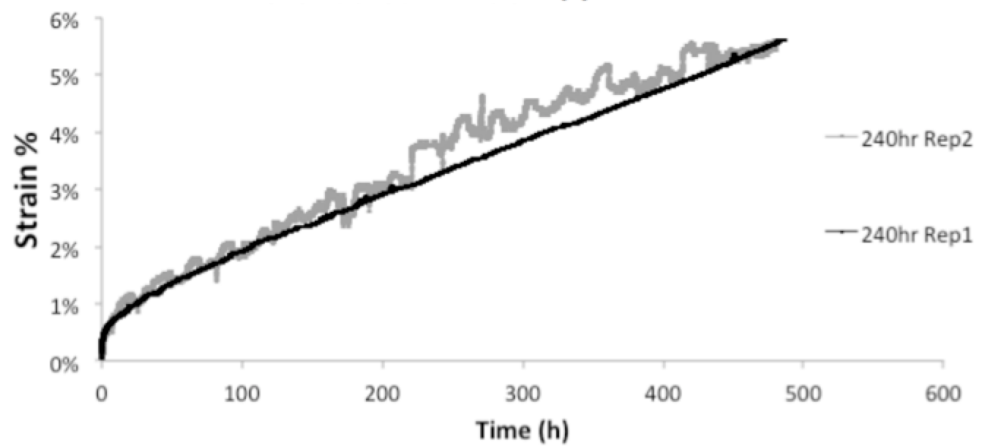
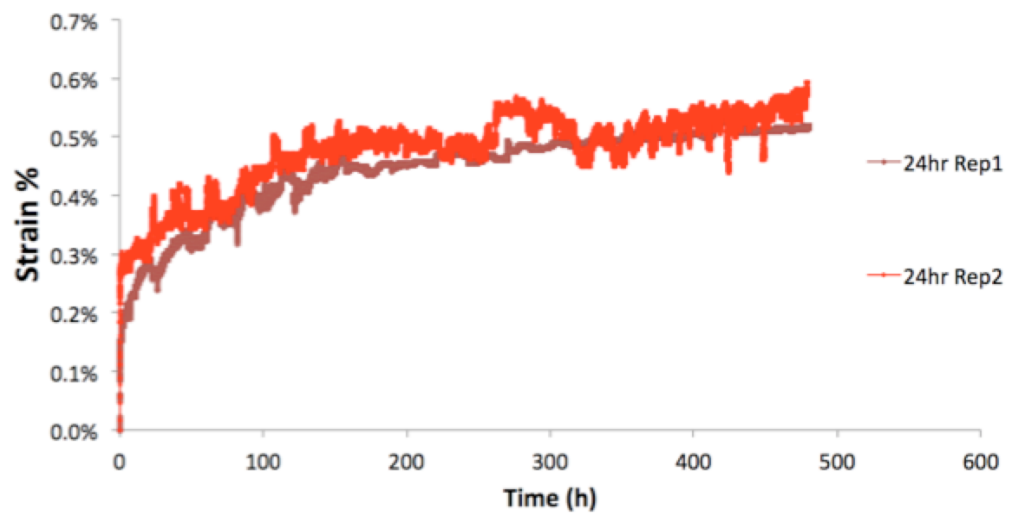
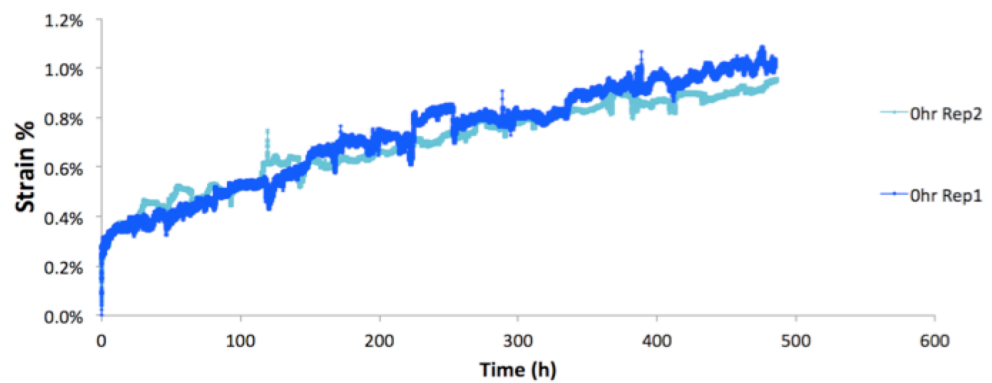




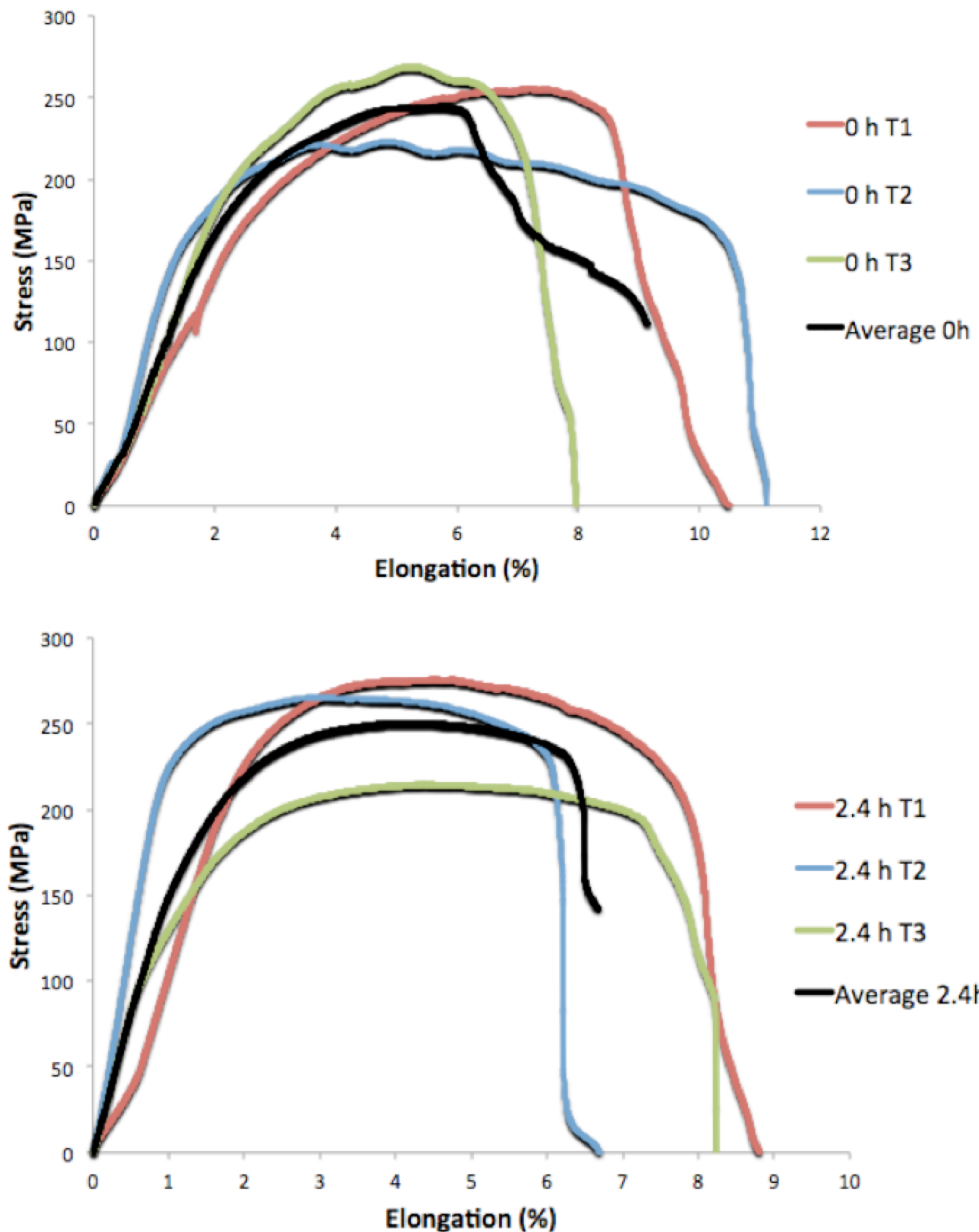


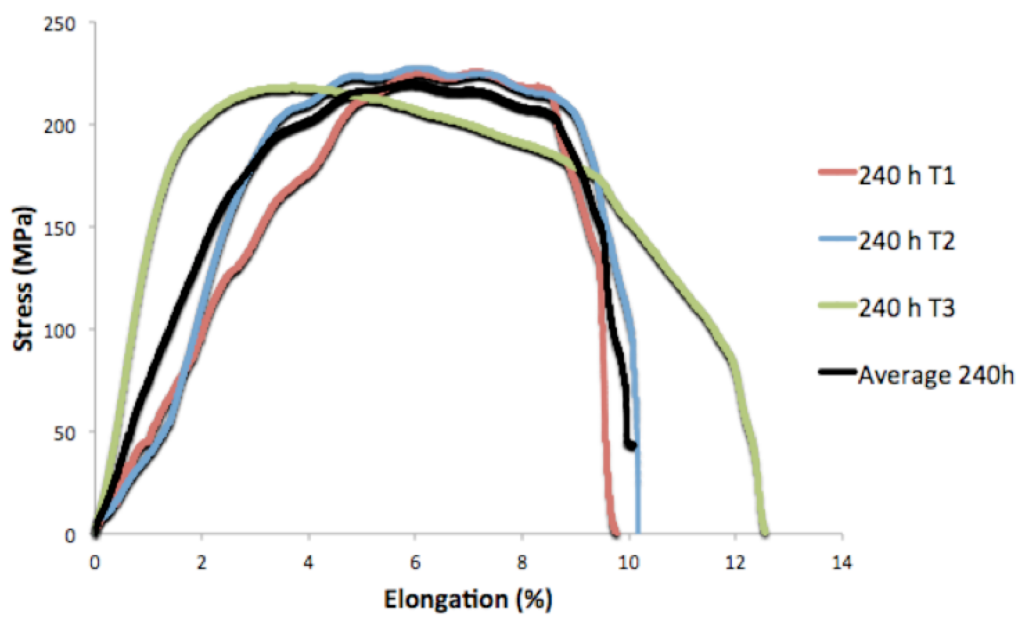
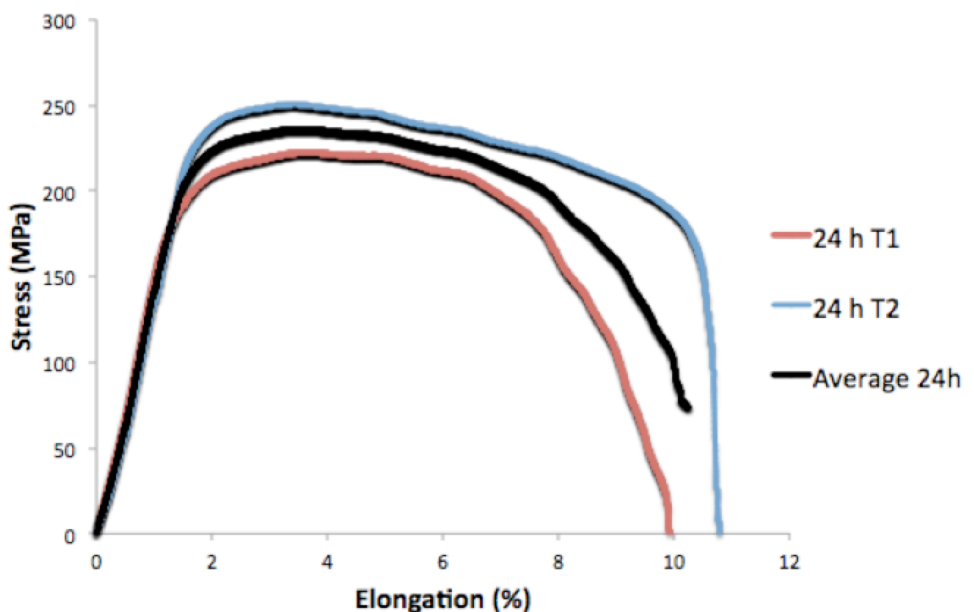
### Appendix III: Additional high temperature constant-stress creep curves for each aging condition





#### Appendix IV: Additional high temperature tensile test curves for each aging condition





## 7 REFERENCES

1. Viswanathan, R., Armor, A. & BOORAS, G. A critical look at supercritical power plants. *Power* **148**, 42–49 (2004).
2. Viswanathan, R., Coleman, K. & Rao, U. Materials for ultra-supercritical coal-fired power plant boilers. *Int. J. Press. Vessels Pip.* **83**, 778–783 (2006).
3. Viswanathan, V., Purgert, R. & Rawls, P. Coal-fired power materials. *Adv Mater Process* **166**, 47–49 (2008).
4. Viswanathan, R. *et al.* US program on materials technology for ultra-supercritical coal power plants. *J. Mater. Eng. Perform.* **14**, 281–292 (2005).
5. Viswanathan, R. & Bakker, W. Materials for ultrasupercritical coal power plants—Boiler materials: Part 1. *J. Mater. Eng. Perform.* **10**, 81–95 (2001).
6. Holcomb, G. R. *et al.* *Ultra Supercritical Turbines--Steam Oxidation*. (Albany Research Center (ARC), 2004).
7. Shingledecker, D. G. and J. *Advances in Materials Technology for Fossil Power Plants: Proceedings from the Seventh International Conference, October 22-25, 2013 Waikoloa, Hawaii, USA*. (ASM International, 2014).
8. Viswanathan, R. *et al.* U.S. program on materials technology for ultra-supercritical coal power plants. *J. Mater. Eng. Perform.* **14**, 281–292
9. Shingledecker, J. P. & Wright, I. G. *Evaluation of the Materials Technology Required for a 760°C Power Steam Boiler*. (Oak Ridge National Laboratory (ORNL), 2006).

10. Yamamoto, Y. *et al.* Creep-resistant, Al<sub>2</sub>O<sub>3</sub>-forming austenitic stainless steels. *Science* **316**, 433–436 (2007).
11. Viswanathan, R. & Bakker, W. Materials for boilers in ultra supercritical power plants. in *Proceedings of 2000 International Joint Power Generation Conference* **20**, (Miami Beach, Florida, 2000).
12. Yamamoto, Y. *et al.* Alumina-Forming Austenitic Stainless Steels Strengthened by Laves Phase and MC Carbide Precipitates. *Metall. Mater. Trans. A* **38**, 2737–2746 (2007).
13. Brady, M. P., Yamamoto, Y., Santella, M. L. & Pint, B. A. Effects of minor alloy additions and oxidation temperature on protective alumina scale formation in creep-resistant austenitic stainless steels. *Scr. Mater.* **57**, 1117–1120 (2007).
14. Brady, M. P. *et al.* The development of alumina-forming austenitic stainless steels for high-temperature structural use. *JOM* **60**, 12–18 (2008).
15. Pint, B. A., Shingledecker, J. P., Brady, M. P. & Maziasz, P. J. Alumina-forming austenitic alloys for advanced recuperators. *ASME Pap. No GT2007-27916* (2007).
16. Brady, M. P., Yamamoto, Y., Santella, M. L. & Walker, L. R. Composition, microstructure, and water vapor effects on internal/external oxidation of alumina-forming austenitic stainless steels. *Oxid. Met.* **72**, 311–333 (2009).
17. Yamamoto, Y., Santella, M. L., Brady, M. P., Bei, H. & Maziasz, P. J. Effect of Alloying Additions on Phase Equilibria and Creep Resistance of Alumina-Forming Austenitic Stainless Steels. *Metall. Mater. Trans. A* **40**, 1868–1880 (2009).

18. Brady, M. P., Magee, J., Yamamoto, Y., Helmick, D. & Wang, L. Co-optimization of wrought alumina-forming austenitic stainless steel composition ranges for high-temperature creep and oxidation/corrosion resistance. *Mater. Sci. Eng. A* **590**, 101–115 (2014).
19. Yamamoto, Y., Muralidharan, G. & Brady, M. P. Development of L1 2-ordered Ni 3 (Al, Ti)-strengthened alumina-forming austenitic stainless steel alloys. *Scr. Mater.* **69**, 816–819 (2013).
20. Yamamoto, Y. *et al.* Alloying effects on creep and oxidation resistance of austenitic stainless steel alloys employing intermetallic precipitates. *Intermetallics* **16**, 453–462 (2008).
21. Yamamoto, Y. *et al.* Overview of strategies for high-temperature creep and oxidation resistance of alumina-forming austenitic stainless steels. *Metall. Mater. Trans. A* **42**, 922–931 (2011).
22. Kofstad, P. & Bredesen, R. High temperature corrosion in SOFC environments. *Solid State Ion.* **52**, 69–75 (1992).
23. Pint, B. A., Distefano, J. R. & Wright, I. G. Oxidation resistance: One barrier to moving beyond Ni-base superalloys. *Mater. Sci. Eng. A* **415**, 255–263 (2006).
24. Pint, B. A., Peraldi, R. & Maziasz, P. J. The use of model alloys to develop corrosion-resistant stainless steels. in *Materials Science Forum* **461**, 815–822 (Trans Tech Publ, 2004).
25. Brady, M. P. *et al.* *Oxidation resistant high creep strength austenitic stainless steel.* (Google Patents, 2010).

26. Yamamoto, Y., Brady, M. P., Lu, Z. P. & Liu, C. Multi-phase high temperature alloys: exploration of laves-strengthened steels. in *Annual Conference On Fossil Energy Materials* 20–27 (Citeseer, 2006).
27. Cahn, J. W. Nucleation on dislocations. *Acta Metall.* **5**, 169–172 (1957).
28. Porter, D. A., Easterling, K. E. & Sherif, M. *Phase Transformations in Metals and Alloys, (Revised Reprint)*. (CRC press, 2009).
29. Chen, S., Zhang, C., Xia, Z., Ishikawa, H. & Yang, Z. Precipitation behavior of Fe 2 Nb Laves phase on grain boundaries in austenitic heat resistant steels. *Mater. Sci. Eng. A* **616**, 183–188 (2014).
30. Pint, B. A. *et al.* Development of alumina-forming austenitic alloys for advanced recuperators. in *ASME Turbo Expo 2009: Power for Land, Sea, and Air* 271–280 (American Society of Mechanical Engineers, 2009).
31. Sourmail, T. Precipitation in creep resistant austenitic stainless steels. *Mater. Sci. Technol.* **17**, 1–14 (2001).
32. Abe, F., Taneike, M. & Sawada, K. Alloy design of creep resistant 9Cr steel using a dispersion of nano-sized carbonitrides. *Int. J. Press. Vessels Pip.* **84**, 3–12 (2007).
33. Stott, F., Wood, G. & Stringer, J. The influence of alloying elements on the development and maintenance of protective scales. *Oxid. Met.* **44**, 113–145 (1995).
34. Reed, R. C. *The Superalloys: Fundamentals and Applications*. (Cambridge University Press, 2008).

35. Trotter, G., Rayner, G., Baker, I. & Munroe, P. R. Accelerated precipitation in the AFA stainless steel Fe–20Cr–30Ni–2Nb–5Al via cold working. *Intermetallics* **53**, 120–128 (2014).
36. Kato, Y., Ito, M., Kato, Y. & Furukimi, O. Effect of Si on Precipitation Behavior of Nb-Laves Phase and Amount of Nb in Solid Solution at Elevated Temperature in High Purity 17% Cr-0.5% Nb Steels. *Mater. Trans.* **51**, 1531–1535 (2010).
37. Liu, C., Zhu, J., Brady, M., McKamey, C. & Pike, L. Physical metallurgy and mechanical properties of transition-metal Laves phase alloys. *Intermetallics* **8**, 1119–1129 (2000).
38. Trotter, G. & Baker, I. The effect of aging on the microstructure and mechanical behavior of the alumina-forming austenitic stainless steel Fe–20Cr–30Ni–2Nb–5Al. *Mater. Sci. Eng. A* **627**, 270–276 (2015).
39. Cao, W. & Kennedy, R. Superalloys 718, 625, 706 and Various Derivatives, ed. EA Loria *TMS* 455–464 (2001).
40. Massalski, T. B., Murray, J. L., Bennett, L. H. & Baker, H. Binary Alloy Phase Diagrams; American Society for Metals: Metals Park, OH, 1986. *There No Corresp. Rec. This Ref.* (1904).
41. Villars, P., Prince, A. & Okamoto, H. *Handbook of ternary alloy phase diagrams*. (Asm Intl, 1995).
42. Tarigan, I., Kurata, K., Takata, N., Matsuo, T. & Takeyama, M. Novel Concept of Creep Strengthening Mechanism using Grain Boundary Fe 2 Nb Laves Phase in Austenitic Heat Resistant Steel. in *MRS Proceedings* **1295**, mrsf10–1295 (Cambridge Univ Press, 2011).

43. Tarigan, I., Takata, N. & Takeyama, M. Grain boundary precipitation strengthening mechanism by Fe<sub>2</sub>Nb Laves phase in creep of Fe-20Cr-30Ni-2Nb austenitic heat resistant steel. in *Proceedings of the 12th International Conference on Creep and Fracture of Engineering Materials and Structure (JIMIS 11)* (2012).
44. Brady, M. P. *et al.* On the loss of protective scale formation in creep-resistant, alumina-forming austenitic stainless steels at 900 C in air. in *Materials Science Forum* **595**, 725–732 (Trans Tech Publ, 2008).
45. Satyanarayana, D., Malakondaiah, G. & Sarma, D. Characterization of the age-hardening behavior of a precipitation-hardenable austenitic steel. *Mater. Charact.* **47**, 61–65 (2001).
46. Satyanarayana, D., Malakondaiah, G. & Sarma, D. Steady state creep behaviour of NiAl hardened austenitic steel. *Mater. Sci. Eng. A* **323**, 119–128 (2002).
47. Garofalo, F., Richmond, O. & Domis, W. F. Design of apparatus for constant-stress or constant-load creep tests. *J. Basic Eng.* **84**, 287–293 (1962).
48. da C. Andrade, E. N. & Chalmers, B. The Resistivity of Polycrystalline Wires in Relation to Plastic Deformation, and the Mechanism of Plastic Flow. *Proc. R. Soc. Lond. Math. Phys. Eng. Sci.* **138**, 348–374 (1932).
49. Kanno, N., Yoshimura, K., Takata, N., Tarigan, I. & Takeyama, M. Mechanical properties of austenitic heat-resistant Fe–20Cr–30Ni–2Nb steel at ambient temperature. *Mater. Sci. Eng. A* **662**, 551–563 (2016).

50. Hu, B. *et al.* The Effects of Cold Work on the Microstructure and Mechanical Properties of Intermetallic Strengthened Alumina-Forming Austenitic Stainless Steels. *Metall. Mater. Trans. A* **46**, 3773–3785 (2015).
51. Yukinori Yamamoto *et al.* Development of Alumina-Forming Austenitic Stainless Steels =Multi-Phase High-Temperature Alloys=. in *Materials Science and Technology Division* (Oak Ridge National Laboratory, 2008).
52. Zhou, D. Q. *et al.* Plastic flow behaviour in an alumina-forming austenitic stainless steel at elevated temperatures. *Mater. Sci. Eng. A* **594**, 246–252 (2014).
53. Martin, J. W. *Precipitation Hardening: Theory and Applications*. (Butterworth-Heinemann, 2012).
54. Shi, D., Dong, C. & Yang, X. Constitutive modeling and failure mechanisms of anisotropic tensile and creep behaviors of nickel-base directionally solidified superalloy. *Mater. Des.* **45**, 663–673 (2013).
55. Bei, H., Yamamoto, Y., Brady, M. P. & Santella, M. L. Aging effects on the mechanical properties of alumina-forming austenitic stainless steels. *Mater. Sci. Eng. A* **527**, 2079–2086 (2010).
56. Bird, J. E., Mukherjee, A. K. & Dorn, J. E. *Correlations Between High-Temperature Creep Behavior and Structure*. (California Univ., Berkeley. Lawrence Radiation Lab., 1969).